國 立 交 通 大 學

光電工程學系碩士班

碩 士 論 文

非晶/結晶矽量子點埋入式氧化鋅薄膜

之開發與於光伏元件之應用

Development of amorphous- and crystalline-Si quantum dots

embedded ZnO thin films for photovoltaic device application

研 究 生：劉權政

指導教授：李柏璁 博士

中 華 民 國 一百零一 年 十 月

非晶/結晶矽量子點埋入式氧化鋅薄膜

之開發與於光伏元件之應用

Development of amorphous- and crystalline-Si quantum dots embedded ZnO thin films for photovoltaic device application

研 究 生：劉權政　　Student：Chaun-Cheng Liu

指導教授：李柏璁　博士　　Advisor：Dr. Po-Tsung Lee

國 立 交 通 大 學

光電工程學系碩士班

碩 士 論 文

A Thesis

Submitted to Department of Photonic and Institute of Electro-Optical Engineering

College of Electrical Engineering and Computer Science

National Chiao Tung University

In partial Fulfillment of the Requirements

for the Degree of Master

in

Department of Photonic and Electro-Optical Engineering

October 2012

Hsinchu, Taiwan, Republic of China

中華民國一百零一年十月

非晶/結晶矽量子點埋入式氧化鋅薄膜

之開發與於光伏元件之應用

研 究 生：劉權政

指導教授：李柏璁 博士

國立交通大學光電工程學系碩士班

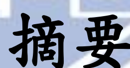

摘要

近年來，由於矽量子點薄膜具有可大範圍調控能隙與獨特的光學特性，故已被廣泛研究並應用於多種熱門光電元件，其中於光伏元件之應用亦被視為相當具有潛力的研究之一，因其將可解決目前全矽基組成太陽能電池於短波長波段具有較大能量損耗的問題。目前矽量子點薄膜主要以矽相關介電材料為矩陣材料，雖已驗證其具有明顯光伏特性，但其特性仍受限於矩陣材料的高阻值特性，導致整體光電效益尚無法達到預期。有鑒於目前矽量子點薄膜應用太陽能電池所遭遇的瓶頸，我們提出以氧化鋅為矽量子點矩陣材料，因其不但具有矩陣材料所需必備的寬能隙特性，同時更具有高光穿透度與高度可調的電性特性，故若能成功整合矽量子點與氧化鋅薄膜，必可大幅提升矽量子點薄膜整合於太陽能電池的光電效益。此篇論文中，我們利用射頻濺鍍薄膜沉積方式，成長二十週期的[氧化鋅/矽]多層膜結構，藉由一高矽濺鍍功率與矽薄層厚度調控，於室溫下沉積出自組織矽量子點埋入式氧化鋅薄膜，並分析該薄膜於不同退火溫度下，其結晶特性、光學特性與電性特性。此外，我們亦利用調控適當的退火時間與氫退火製程，分別針對非晶與結晶矽量子點薄膜做更進一步的光電特性優化，未來若能有效整合矽量子點薄膜與非晶/微晶矽薄膜，將可邁向全矽基組成之高效率與低成本的第三代薄膜太陽能電池。

Development of Amorphous- and Crystalline-Si Quantum Dots Embedded ZnO Thin Films for Photovoltaic Device Application

Student : Chuan-Cheng Liu
Advisor : Prof. Po-Tsung Lee

Department of Photonics and Institute of Electro-Optical Engineering,
National Chiao Tung University

Abstract

Recently, the silicon quantum dot (Si QD) thin films have been extensively studied and applied to the popular optoelectronics due to the widely tunable bandgap and unique optical properties. For example, the Si QD thin films have the great potential for photovoltaic (PV) applications because it can solve the optical loss problem in the short-wavelength range for the Si-based solar cells (SCs). So far, the Si-based dielectric materials are used as the matrix material of Si QD, and the PV properties has been demonstrated. However, the overall PV properties are still limited by the naturally high resistance of the Si-based dielectric matrix materials. In order to solve the bottleneck of the Si QD thin films applying to SC application, we propose to use ZnO as the matrix material of Si QDs since the ZnO thin film is a semiconductor material with wide bandgap, high transparency, and tunably electrical properties. These advantages are potential in improving the electro-optical properties of the Si QD thin films for SC application. In this study, the Si QD embedded ZnO thin films are fabricated by sputtering method and deposited by a [ZnO/Si] multilayer structure with 20 pairs. The self-assembled Si nano-clusters are formed in ZnO matrix by high Si sputtering power and thin Si layer thickness during deposition. The crystalline, optical, and electrical properties of the samples annealed at different temperatures are investigated and discussed. Besides, the electro-optical properties of the amorphous- and crystalline-Si QD thin films are also further improved by tuning the annealing time and using the H_2 annealing process. The all Si-based third generation solar cells with high efficiency and low cost can be highly expected by integrating the Si QD embedded ZnO thin films and the a- or μc-Si thin films in the future.

Acknowledgement

兩年的研究生活倏忽即逝，轉眼已到編寫這段文字的時刻，這兩年中無論是實驗的摸索與學習亦或生活中的笑顏與淚水都盡情的填滿我腦中的每一個記憶空間，讓我經歷了一段深刻且豐富的人生體驗。

首先誠摯的感謝指導教授李柏璁老師兩年來悉心的指導與照顧，在書報討論中學到研究所需技巧以及重要的研究心態，歷來種種皆使我獲益良多。感謝口試委員劉伯村教授、孫建文教授和林國瑞教授在百忙之中抽空指導以及諸多建議，使本論文更趨完整。

在此感謝實驗室所有夥伴陪伴、支持與指導: 感謝光揚學長不厭其煩的指出我研究中的缺失，且總能在我迷惘時為我解惑。感謝贊博、岳哥、家揚、佐哥、佳裕在實驗過程中給予我的寶貴意見。已畢業的學長姊們金剛、文齡、邱立勛、林雋崴、呂紹平不論是操作機台或問題討論都有莫大的幫助。感謝 ping、小智、哲嶢、開昊的支持與鼓勵，尤其感謝 ping 的大力協助，幫助我事半功倍。小幫手陳酷哥當然也不能忘記，感謝你的幫忙及搞笑。也期望在未來的路途中，能將所遭遇到的辛苦與挫折，轉化成前進的動力，繼續朝下一目標邁進。

最後，謹以此文獻給我摯愛的雙親。感謝我的家人，在這段時間裡，一直守護著我，讓我能全心全意完成碩士學業。

劉權政。2012 年 11 月 謹誌於 國立交通大學

Content

摘要 ... I
Abstract ... II
Acknowledgement ... III
Content ... IV
List of Figure ... VI
List of Table ... X
Chapter 1 Introduction ... 1
1.1 Background ... 1
1.2 Limitation of Solar Cell Efficiency ... 2
1.3 Principle of Si QD Thin Film ... 4
1.4 Si QD Embedded in Dielectric Matrix Materials ... 6
1.5 Motivation ... 9
1.6 Characteristic of ZnO Material ... 10
Chapter 2 Sample Fabrication and Equipment ... 11
2.1 Sample Fabrication ... 11
2.1.1 Substrates Clean ... 11
2.1.3 Thin Film Deposition ... 11
2.1.4 Post-Annealing Process ... 12
2.1.5 Electrode Deposition ... 13
2.2 Equipment ... 14
2.2.1 AFM Image ... 14
2.2.2 SEM Image ... 15
2.2.3 TEM Image ... 16
2.2.4 Raman Spectrum ... 18

1896

2.2.5 XRD Pattern....20
2.2.6 UV-Vis-NIR Spectrum....23
2.2.7 I-V Curve....23
Chapter 3 Results and Discussions....25
3.1 [ZnO/Si] Multilayer Thin Films....25
3.1.1 Structural Properties....25
3.1.2 Crystalline Properties of Si QDs....26
3.1.3 Crystalline Properties of ZnO Matrix....28
3.1.4 Film Stress....30
3.1.5 Optical Properties....31
3.1.6 Electrical Properties....32
3.2 a-Si QDs embedded ZnO thin films....36
3.2.1 Crystalline Properties....36
3.2.2 Electrical Properties....37
3.3 a-Si QDs embedded ZnO thin films with H_2 annealing....39
3.3.1 Crystalline and Optical Properties....39
3.3.2 Electrical Properties....40
3.4 c-Si QDs embedded ZnO thin films....42
3.4.1 Crystalline Properties....42
3.4.2 Electrical Properties....43
3.5 c-Si QDs embedded ZnO thin films with H_2 annealing....45
3.5.1 Crystalline and Optical Properties....45
3.5.2 Electrical Properties....46
Chapter 4 Conclusion....48
Reference....49

List of Figure

Chapter 1

Fig 1. 1 Classification of three generation solar cells and its cost per peak watt ($/Wp). [5] 1

Fig 1. 2 Energy loss mechanisms of a single pn junction Si solar cell. 2

Fig 1. 3 Formation of energy levels from quantum confinement effect. 4

Fig 1. 4 Relation between the effective bandgap and QD size by using SiO_2 and Si_3N_4. [9] 5

Fig 1. 5 Formation of nc-Si QDs embedded in the Si-based dielectric matrix materials by a multilayer thin film structure. 6

Fig 1. 6 Bulk band diagram between crystalline silicon and its carbide, nitride and oxide matrix. 7

Fig 1. 7 Schemes of the p-i-n Si QD thin film solar cell. 7

Fig 1. 8 I–V characteristics of the p-i-n Si QD thin film solar cell under 1-sun illumination. 8

Fig 1. 9 Optical and electrical properties of ZnO material: (a) absorption coefficient, (b) transmittance, (c) resistivity, (d) mobility, and (e) carrier concentration. 10

Chapter 2

Fig 2. 1 Fabrication flow of the Si QD thin films. 11

Fig 2. 2 Diagram of ZnO/Si ML thin film structure. 12

Fig 2. 3 Illustration of the as-deposited and annealed [ZnO/Si] ML thin films. 13

Fig 2. 4 Diagrams of (a) the square mask for the front electrode and (b) the device structure. 13

Fig 2. 5 Illustration of scanning method by AFM. 14

Fig 2. 6 Image of the cantilever tip for AFM measurement. [20] 14

Fig 2. 7 Diagram of interaction between incident electron beam and sample. 15

Fig 2. 8 Imaging principle of phase contrast. 16

Fig 2. 9 Diffraction pattern of face-centered cubic (fcc) crystal. 16

Fig 2. 10 Imaging methods of diffraction contrast: (a) bright field image and (b) dark field image. 17

Fig 2. 11 (a) Bright field image and (b) dark field image of a BF^+ ion implantation sample. 17

Fig 2. 12 Energy transfer of Raman effect. 18

Fig 2. 13 Diagram of Raman energy transition. 19

Fig 2. 14 Diagram of Bragg's diffraction. 21

Fig 2. 15 Diagram of θ-2θ scanning method. 22

Fig 2. 16 Diagram of grazing incident X-ray diffraction. 22

Chapter 3

Fig 3. 1 Surface morphologic images of the as-deposited ZnO (5 nm) and ZnO(5 nm)/Si(3 nm) thin films by AFM. 25

Fig 3. 2 (a) Low magnification and (b) high magnification HRTEM images of the as-deposited [ZnO/Si] ML thin films. 26

Fig 3. 3 Raman spectra of the annealed ML thin films under different annealing temperature for 30 minutes. 27

Fig 3. 4 The curve-fitting result of Raman spectrum for sample F1000. 27

Fig 3. 5 (a) Crystallinity and integrated intensity and (b) FWHM and peak position for the nc-Si QDs from Raman spectra. 28
Fig 3. 6 XRD patterns of the annealed ML samples. Inset shows the XRD pattern from 20 to 60° for sample F300. 29
Fig 3. 7 Integrated intensities of the normal, stressed, and total ZnO(002) for the annealed samples..30
Fig 3. 8 SEM images of the samples annealed at (a) 500°C and (b) 1000 ^{o}C for 30min...31
Fig 3. 9 Ratio of bending area and bending density of the annealed samples. 31
Fig 3. 10 (a) Absorbance and (b) transmittance of the annealed samples....32
Fig 3. 11 Band diagrams of p-type Si wafer and n-type ZnO material (a) before and (b) after combination and (c) the I-V curve of the hetero-junction cell. 33
Fig 3. 12 Dark I-V curves of the annealed samples. 34
Fig 3. 13 (a) Turn-on voltage and (b) vertical resistivity of the annealed samples..34
Fig 3. 14 Light I-V curves of the annealed samples. 35
Fig 3. 15 (a) Open circuit voltage and (b) short circuit current of the annealed samples..35
Fig 3. 16 (a) Raman spectra and (b) XRD patterns of the samples annealed at 500 ^{o}C under different annealing time. 37
Fig 3. 17 (a) Dark and (b) light I-V curves of the samples annealed at 500 ^{o}C under different annealing time. 38
Fig 3. 18 (a) Raman spectra and (b) XRD patterns of the annealed samples

after N_2 and H_2 annealing. 40
Fig 3. 19 (a) Absorbance and (b) transmittance of the annealed samples after N_2 and H_2 annealing. 40
Fig 3. 20 (a) Dark and (b) light I-V curves of the annealed samples after N_2 and H_2 annealing. 41
Fig 3. 21 (a) Raman spectra and (b) XRD patterns of the samples annealed at 700 ^oC under different annealing time. 42
Fig 3. 22 Film bending density of the samples annealed at 700 ^oC under different annealing time. 43
Fig 3. 23 (a) Dark and (b) light I-V curves of the samples annealed at 700 ^oC under different annealing time. 44
Fig 3. 24 (a) Raman spectra and (b) XRD patterns of the annealed samples after N_2 and H_2 annealing. 45
Fig 3. 25 (a) Dark and (b) light I-V curves of the samples after N_2 and H_2 annealing. 46

List of Table

Table 1. 1 Energy loss simulation for 1.3 eV bandgap. [7]............................3

Table 3. 1 Parameters for the crystalline properties of Si QDs under different annealing temperature...28

Table 3. 2 Crystalline properties of ZnO(002) for the annealed samples. ...30

Table 3. 3 Curve-fitting results for the crystalline properties of ZnO matrix of the samples annealed at 500 ^{o}C under different annealing time. 37

Table 3. 4 Parameters from I-V curves of the samples annealed at 500 ^{o}C under different annealing time. 38

Table 3. 5 Parameters from I-V curves of the annealed samples after N_2 and H_2 annealing...41

Table 3. 6 Curve-fitting results from XRD patterns of the samples annealed at 700 ^{o}C under different annealing time. 43

Table 3. 7 Parameters from I-V curves of the annealed samples at 700 ^{o}C under different annealing time. 44

Table 3. 8 Curve-fitting results from Raman spectra and XRD patterns of the annealed samples after N_2 and H_2 annealing. 46

Table 3. 9 Parameters from I-V curves of the annealed samples after N_2 and H_2 annealing...47

Chapter 1 Introduction

1.1 Background

Recently, the green energy requirements are substantially increased due to the environment population and the technology development, and solar cell is one kind of the important green energies. The solar cells can be classified into three types, as shown in Fig 1. 1. The first generation solar cells are high efficiency and high cost like the c-Si bulk solar cell. Second generation solar cells are low cost and low efficiency like the organic solar cell. The present limitation of solar cells is about 40% and their costs per watt are still surcharge.[1] Therefore, the third generation solar cells with high efficiency and low cost are needed like the dye-sensitized solar cell and the tandem solar cell.[2-4]. It has the higher efficiency limitation about 60% and the cost is expected to be lower than 0.5 $/W. The nano-crystalline Si quantum dot thin films with tunably effective bandgap and good optical properties are great potential for the third generation solar cell application.

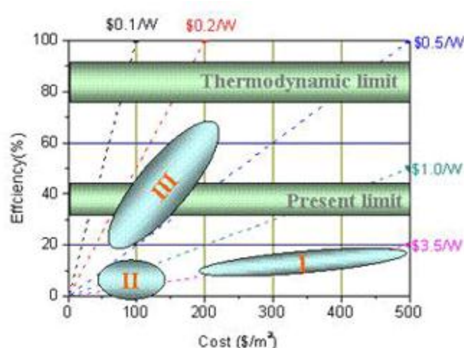

Fig 1. 1 Classification of three generation solar cells and its cost per peak watt ($/Wp). [5]

1.2 Limitation of Solar Cell Efficiency

Fig 1. 2 shows the energy loss mechanisms of a single pn junction Si solar cell. Such as the (1) thermalization loss, (2) junction voltage loss, (3) recombination loss, and (4) contact voltage loss. The larger energy of incident light than Si bandgap will lead to the obvious thermalization loss and limit the highest conversion efficiency <44%, hence, it’s one of the critical energy loss mechanisms. We can cascade different bandgap materials to decrease thermal loss. Recombination loss is also an important loss mechanism and we can choose long life-time photo-excited carrier and perfect lattice material to decrease it. Shockley and Queisser explore the relation of ideal solar cell emission and blackbody radiation and the 1.3 eV bandgap of solar cell that has 31% conversion is derived. [6] The 31% conversion is lower than previous 44% efficiency because the lower output voltage is limited by junction voltage loss and contact voltage loss. Output voltage is lower than theoretical energy bandgap. We can decrease junction voltage loss and contact voltage loss to improve efficiency by condensing sunlight.

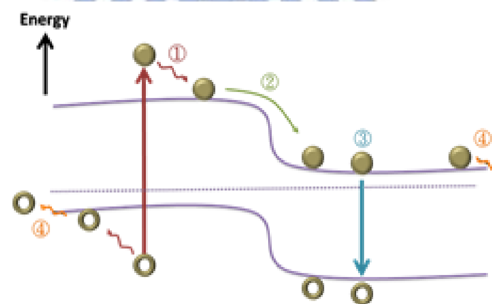

Fig 1. 2 Energy loss mechanisms of a single pn junction Si solar cell.

From above discussion, junction voltage loss, contact voltage loss and recombination loss can be improved by easier methods but the thermalization loss

improvement is difficult. Table 1. 1 shows energy loss simulation of 1.3eV bandgap. Thermal loss is a major loss in Table 1. 1 and it needs different bandgaps to decrease thermalization loss. For Si material, the bandgap of different type Si material is between 1.12 and 1.7eV. To further decrease thermal loss, the higher bandgap is needed. So, Si quantum dot (QD) technology is proposed to reach higher bandgap of Si-based solar cell.

Table 1. 1 Energy loss simulation for 1.3 eV bandgap. [7]

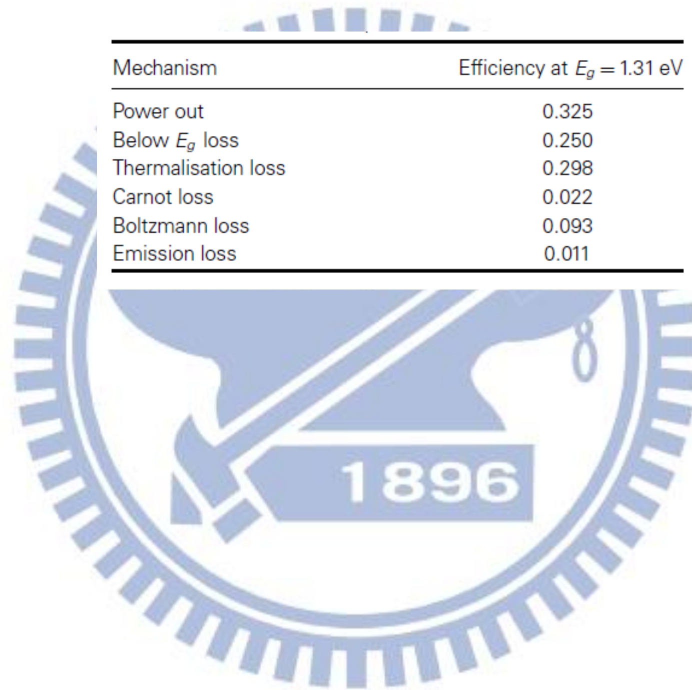

Mechanism	Efficiency at $E_g = 1.31$ eV
Power out	0.325
Below E_g loss	0.250
Thermalisation loss	0.298
Carnot loss	0.022
Boltzmann loss	0.093
Emission loss	0.011

1.3 Principle of Si QD Thin Film

A narrow definition of quantum dots scales is less than 10 nanometers of the zero-dimensional dots. The electrons and holes are confined in a tiny three-dimensional energy barrier when the crystal bulk size reduces below de Broglie wavelength of free electrons. In addition, quantum dot is formed by a few atoms and its electronic density of states is between atoms and bulk due to quantum confinement effect. In Fig 1. 3, quantum confinement leads discontinuous electron energy level that is similar with atomic structure. Therefore, the physical properties of the quantum dots are different from the macroscopic nature. [8] The electronic density of state changes with the dot size, and that will affect its optical, electrical, and magnetic properties.

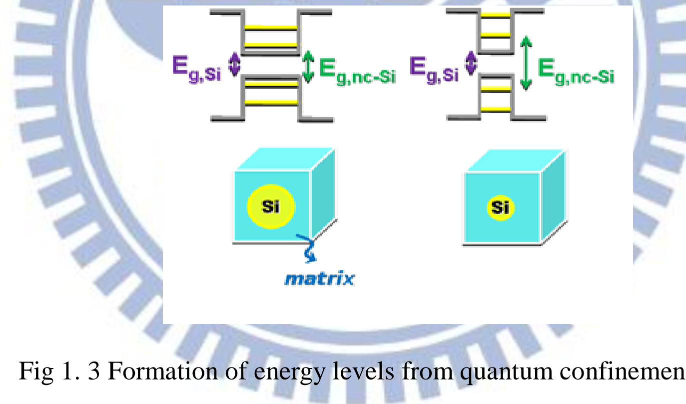

Fig 1. 3 Formation of energy levels from quantum confinement effect.

According to the quantum confinement effect, the nc-Si QD thin film can achieve the larger effective bandgap than a-Si. In addition, it’s highly tunable by tuning the QD size. Fig 1. 4 shows the effective bandgap increasing with decreasing QD size in SiO_2 and Si_3N_4 matrixes. So, it demonstrates the possibility on tunable Si bandgap by Si QD. The multi-junction Si-based solar cells with optimized light absorption can be reached by integrating Si QDs for decreasing the thermalization loss.

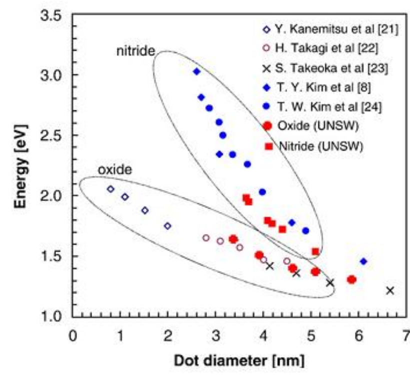

Fig 1. 4 Relation between the effective bandgap and QD size by using SiO_2 and Si_3N_4. [9]

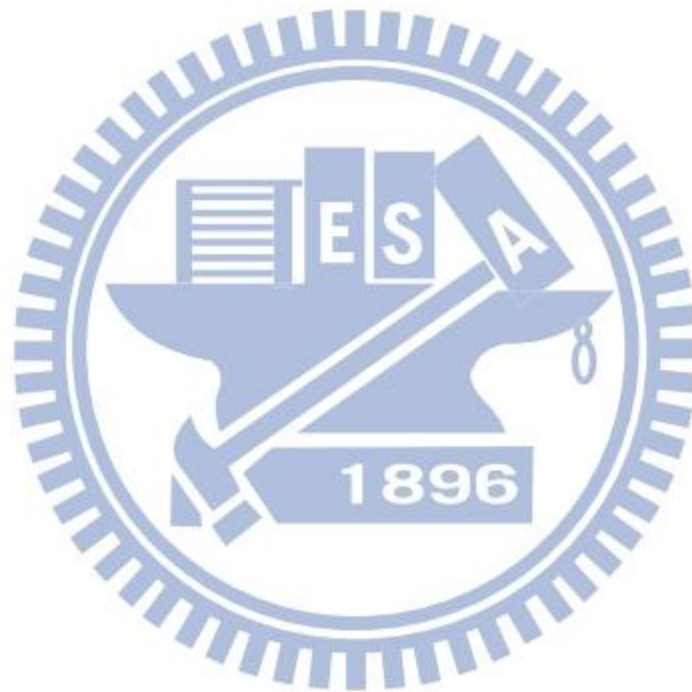

1.4 Si QD Embedded in Dielectric Matrix Materials

The effective bandgap of Si can be largely tuned by using a QD nano-structure. Therefore, the Si QD thin film has potential for LED, memory device, photovoltaic applications and so on. [10, 11] So far, Si QDs are developed by using the Si-based SiO_2, Si_3N_4 and SiC matrix materials. The Si precipitation mechanism can be expressed as equation (1-1) [12]:

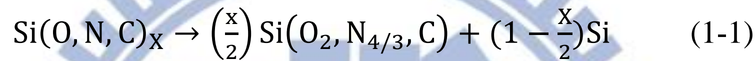

$$\mathrm{Si(O,N,C)_X} \rightarrow \left(\frac{x}{2}\right)\mathrm{Si}\left(\mathrm{O_2}, \mathrm{N_{4/3}}, \mathrm{C}\right) + \left(1-\frac{X}{2}\right)\mathrm{Si} \qquad (1\text{-}1)$$

The thickness and composition of Si-rich layers are important parameters to tune the QD size in a multilayer thin film structure. In figure 1.6, two materials are repeatedly deposited to form the multilayer structure and the Si-rich atoms are precipitated to form Si QDs during annealing process.

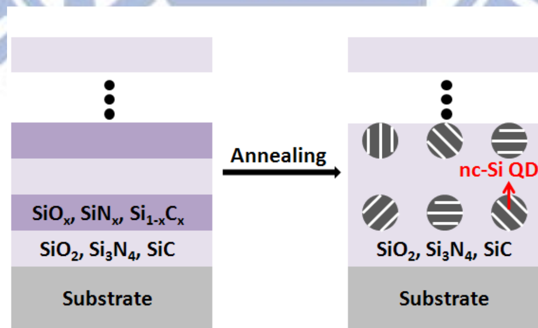

Fig 1. 5 Formation of nc-Si QDs embedded in the Si-based dielectric matrix materials by a multilayer thin film structure.

Fig 1. 6 shows the bulk band diagram between crystalline silicon and its carbide, nitride, and oxide matrices. The tunneling probability is largely dependent on the barrier height.[9, 13, 14] Hence, the matrix materials' properties are critical for the

carrier transport efficiency of the QD thin films.

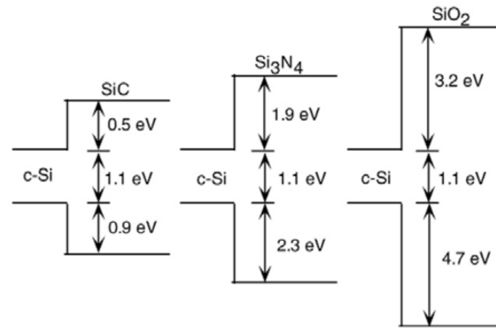

Fig 1. 6 Bulk band diagram between crystalline silicon and its carbide, nitride and oxide matrix.

Fig 1. 7 shows the p-i-n Si QD thin film solar cell fabricated by M. A. Green et al.. It's deposited by alternatively sputtering SiO_2 layer with 2nm and SRO layer 4nm on quartz substrates within-situ boron (B) and phosphorous (P) doping.[15] In Fig 1. 8, it shows the sample has large open circuit voltage about 0.5 V. However, the short circuit current density of ~0.02 mA/cm^2 is largely limited due to the high resistance property of the SiO_2 matrix. The similar results can also be observed in other Si-based dielectric matrix materials such as Si_3N_4 and SiC. [16, 17]

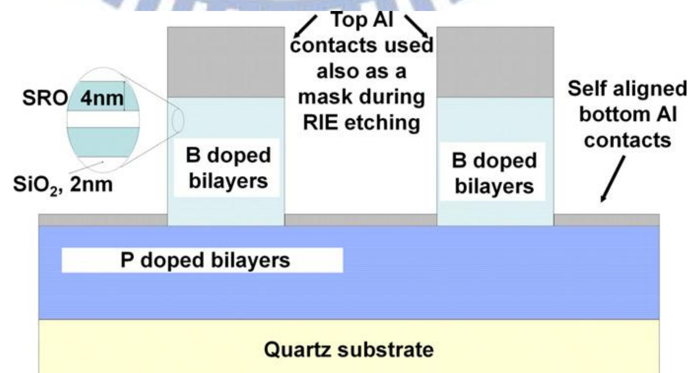

Fig 1. 7 Schemes of the p-i-n Si QD thin film solar cell.

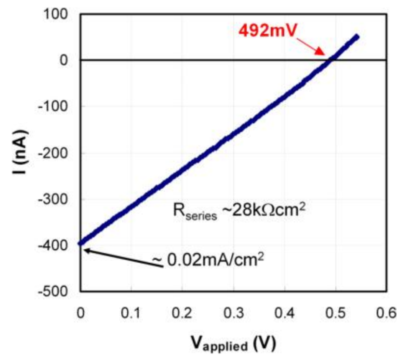

Fig 1. 8 I–V characteristics of the p-i-n Si QD thin film solar cell under 1-sun illumination.

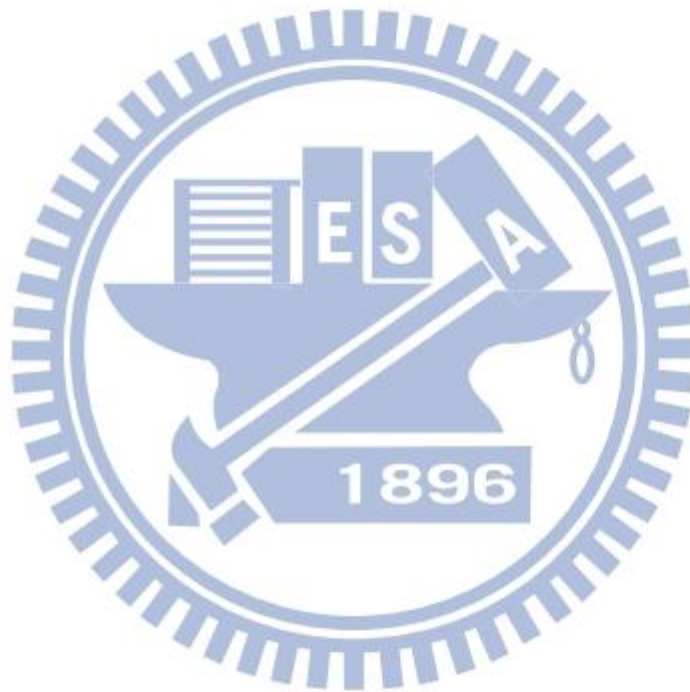

1.5 Motivation

The Si QD thin films with tunable bandgap and good optical properties are great potential in resolving the thermalization loss in the Si-based SC. However, the Si-based dielectric matrix materials will obviously limit the carrier transport efficiency and reduce the device's performance due to their high resistance properties. In order to efficiently improve those problems, we propose to use ZnO as matrix material because ZnO has many suitable properties, such as wide bandgap and high transparency like Si-based dielectric matrices. In addition, it's also a semiconductor with tunable electrical properties. Hence, it has great potential in improving the conductivity than using the Si-based dielectric matrices and efficiently enhancing the device's performance.

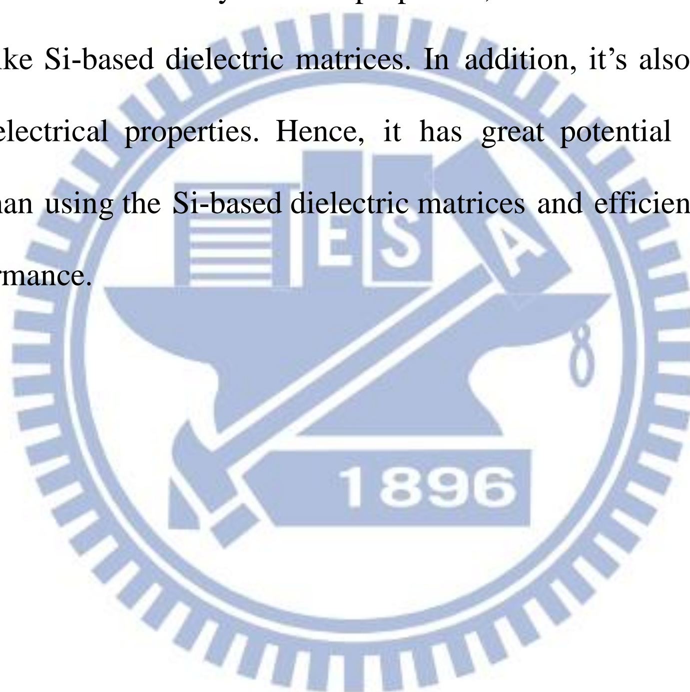

1.6 Characteristic of ZnO Material

ZnO thin film is a Ⅱ-Ⅵ semiconductor material. The wurtzite structure has a hexagonal unit cell with two lattice parameters a and c in the ratio of c/a = 1.633. It has wide bandgap about 3.2~3.4 eV and high transparent, as shown in Fig 1. 9 (a) and (b). Fig 1. 9 (c)~(e) also shows the good electrical properties of resistivity, mobility, and carrier concentration.[18] In addition, the n-type ZnO/ p-type Si hetrojunction solar cell had also been studied by other groups.[19]

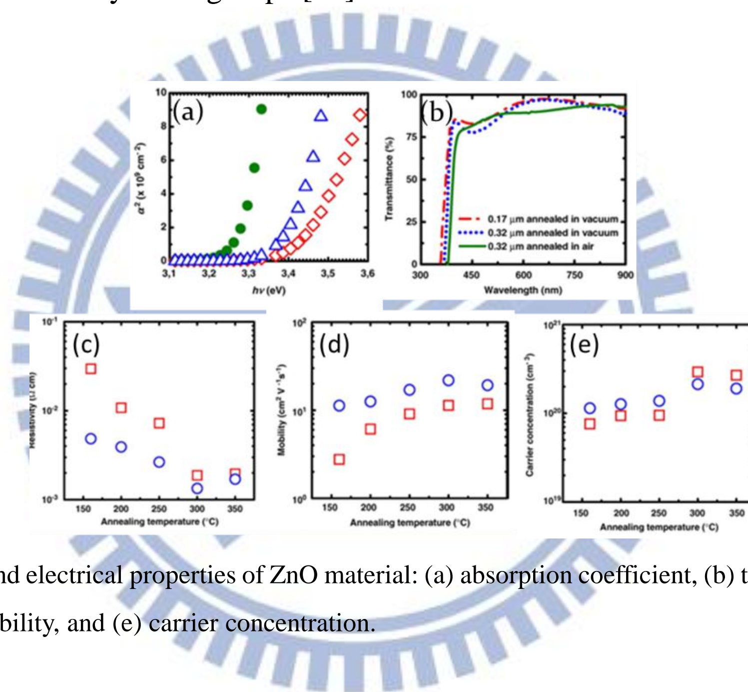

Fig 1. 9 Optical and electrical properties of ZnO material: (a) absorption coefficient, (b) transmittance, (c) resistivity, (d) mobility, and (e) carrier concentration.

Chapter 2 Sample Fabrication and Equipment

2.1 Sample Fabrication

The sample preparation process is introduced in this chapter, Fig 2. 1 shows a brief fabrication flow of the Si QD thin films. The process will be clearly introduced in the next paragraphs.

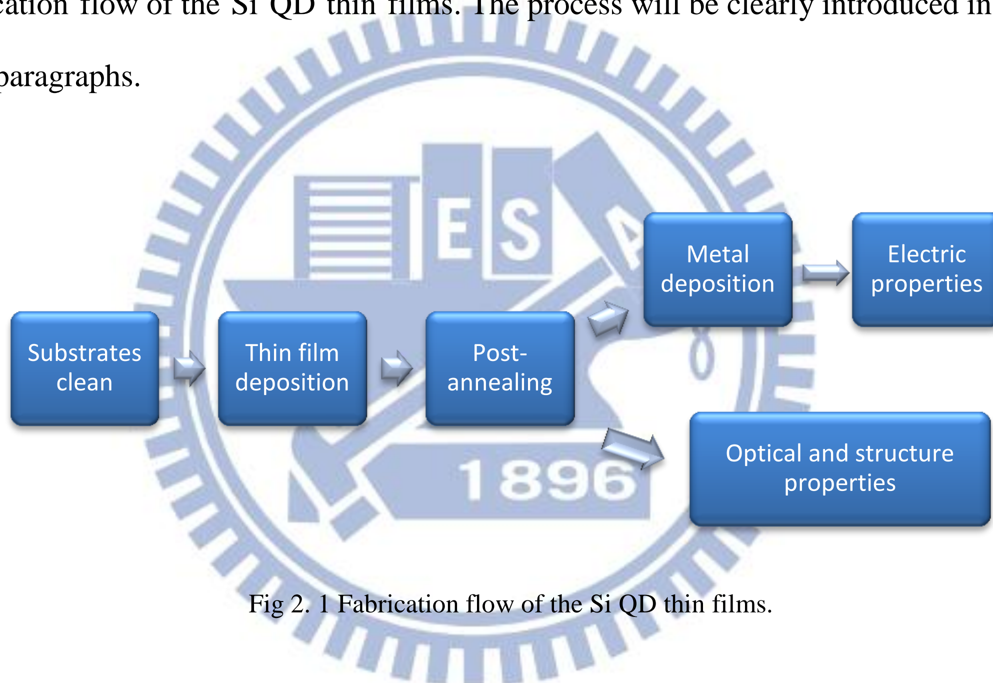

Fig 2. 1 Fabrication flow of the Si QD thin films.

2.1.1 Substrates Clean

The Si wafer is chemically etched with the solutions of H_2SO_4:H_2O_2 = 4:1 at 75℃ for 15 minutes and HF:H_2O = 25:1200 at room temperature for 2 minutes in sequence. The quartzes were ultrasonically cleaned with acetone and alcohol for 10 minutes.

2.1.3 Thin Film Deposition

The radio-frequency (RF) magnetron sputtering method is used to deposit the

ZnO/Si multilayer (ML) thin films. ZnO and Si thin-layers are alternately deposited to form the ML structure, as shown in Fig 2. 2. The base and working pressures are $8*10^{-7}$ torr and $5*10^{-3}$ torr. The sputtering powers of ZnO and Si are fixed at 75 W and 110 W, and the thicknesses are deposited for 5 nm and 3 nm, respectively.

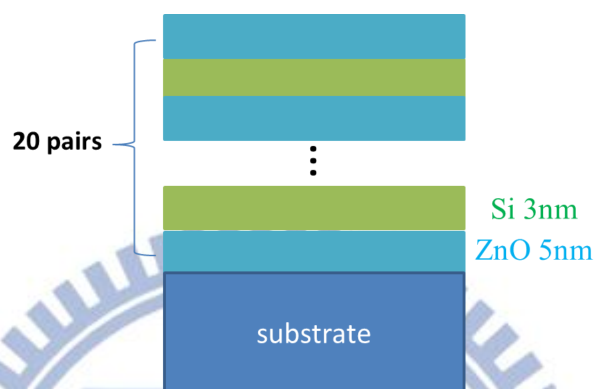

Fig 2. 2 Diagram of ZnO/Si ML thin film structure.

2.1.4 Post-Annealing Process

To improve the crystal quality of the ML thin films, the samples are annealed by furnace in N_2 atmosphere. In our experiment, the samples are annealed between 300 ^oC and 1000 ^oC for 30 minutes to find the proper annealing temperature. Then, we change the annealing time between 30 minutes and 2hr when the proper annealing temperature is selected. Finally, the samples with better electro-optical characteristics are annealed in H_2 atmosphere.

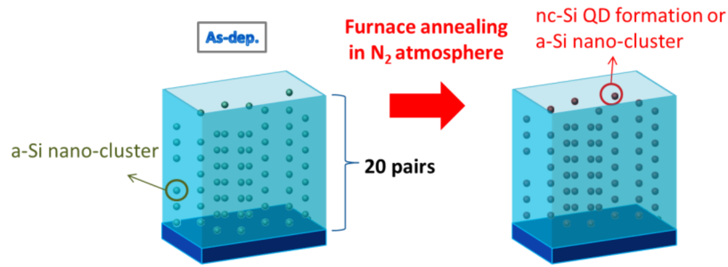

Fig 2. 3 Illustration of the as-deposited and annealed [ZnO/Si] ML thin films.

2.1.5 Electrode Deposition

The Ni film is deposited on the back of sample by thermal coater and 0.8*0.8 cm^2 Al square electrode is deposited on the front of sample by square mask, as shown in Fig 2. 4 (a). Finally, a 200°C annealing for 20minutes is performed for the ohmic contact formation. Fig 2. 4 (b) shows the diagram of the device structure.

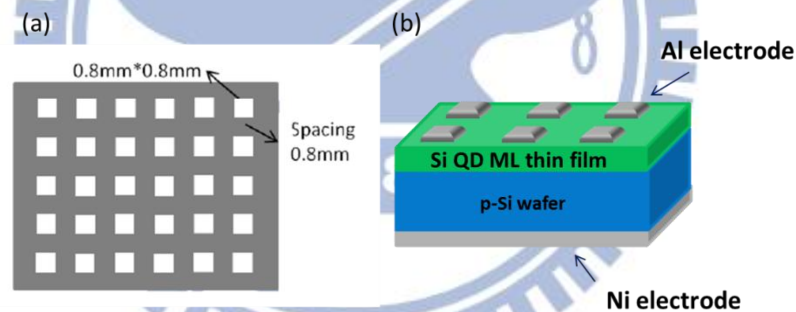

Fig 2. 4 Diagrams of (a) the square mask for the front electrode and (b) the device structure.

2.2 Equipment

2.2.1 AFM Image

The surface morphologies are analyzed by a Digital Instrument D3100 atomic force microscopy (AFM) since it can scan the nano-scaled surface. Generally, there are three scanning modes by using AFM including contact mode, non-contact mode and tapping mode. The contact mode is a high resolution but damaged detection. The non-contact mode is an un-damaged detection but lower resolution. The tapping mode has the advantages of contact and non-contact modes such as the good resolution and nearly un-damaged detection. Hence, the tapping mode is used to scan the sample surface morphologies in our experiment.

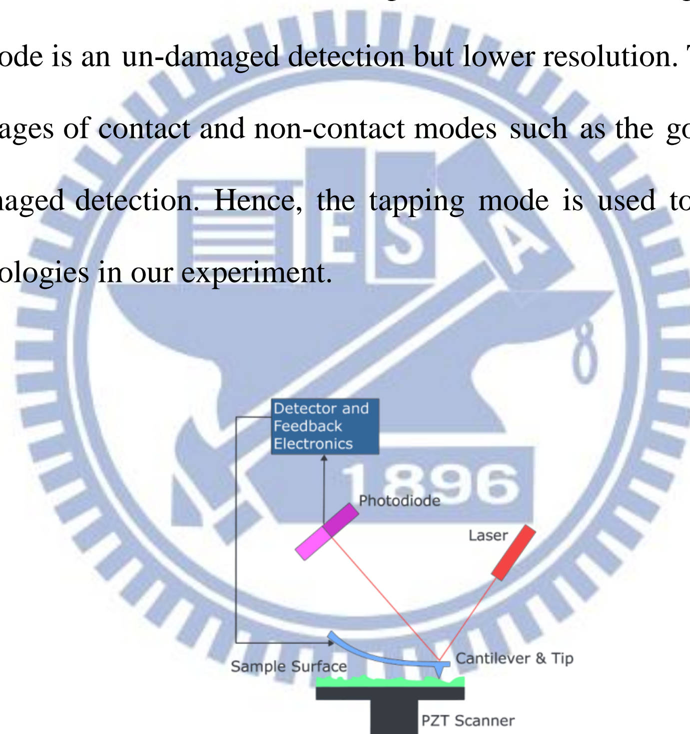

Fig 2. 5 Illustration of scanning method by AFM.

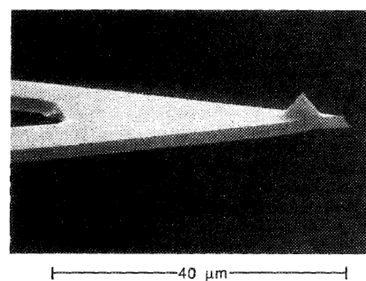

Fig 2. 6 Image of the cantilever tip for AFM measurement. [20]

2.2.2 SEM Image

The scanning electron microscope (SEM) is one of electron microscopes, it uses a focused high-energy electron beam to produce varied signals at the sample surface. The signals produced by the interacting electrons containing the useful information such as the shape, atomic structure, and conductivity. Fig 2. 7 shows the interaction between incident electron beam and sample. When an electron hits the surface, it may be reflected (backscattered), absorbed, or conducted away. The atoms become unstable, give off another electron (a secondary electron), or to give off light in order to stabilize when the atoms absorb electrons. Backscattered electrons and secondary electrons are produced at the surface of sample and SEM can collect these electrons to gain the surface morphology of samples. [20] In the lower conductive samples, the electron beam possibly causes the accumulating charges on the surface to decrease the image resolution, hence, the ultra-thin Au layer is coated to eliminate the accumulating charges in our experiment.

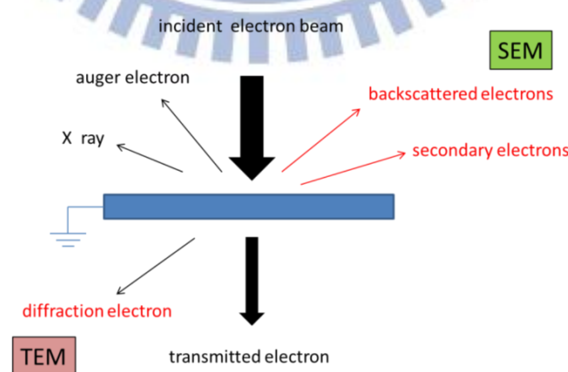

Fig 2. 7 Diagram of interaction between incident electron beam and sample.

2.2.3 TEM Image

The transmission electron microscopy (TEM) is a microscopy technique using a tunneling electron beam through an ultra-thin specimen and interacting with the sample. An image is formed from the interaction of the electrons transmitted through the sample. The image is magnified and focused onto an imaging device, such as a fluorescent screen, on a layer of photographic film, or to be detected by a sensor such as a CCD camera. There are two ways of TEM images including phase contrast and diffraction contrast. Fig 2. 8 shows the imaging principle of phase contrast. [20] Direction electron beam and diffraction electron beam are combined by lens to form phase contrast image. Phase contrast image is different with crystal structure of sample. Fig 2. 9 shows the diffraction pattern of face-centered cubic (fcc) structure.

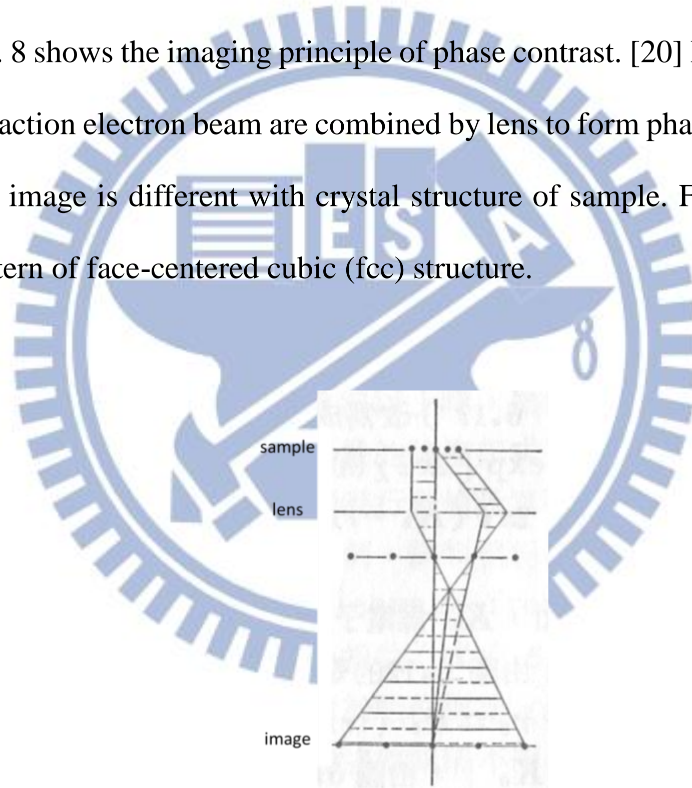

Fig 2. 8 Imaging principle of phase contrast.

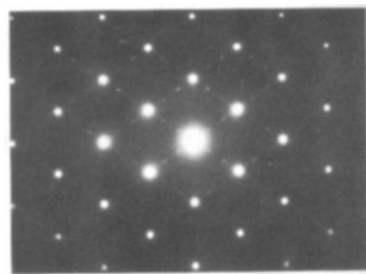

Fig 2. 9 Diffraction pattern of face-centered cubic (fcc) crystal.

Diffraction contrast can be classified to bright field image and dark field image. Fig 2. 10 shows the imaging principle of diffraction contrast. In Fig 2. 10 (a), diffraction electron beam is screened by object aperture, the bright field image is formed by direct electron beam. Fig 2. 10 (b) shows the principle of dark field image, the dark field image is formed by diffraction electron beam. The name of bright and dark field images originate from the high contrast of images. Fig 2. 11 shows the bright and dark field images of BF^+ ion implantation.

TEM is capable of imaging at a significantly higher resolution than optical microscopes owing to the smaller de Broglie wavelength of electrons. This enables the instrument's user to examine fine detail—even as small as a single column of atoms, which is tens of thousands times smaller than the smallest resolvable object in a light microscope.

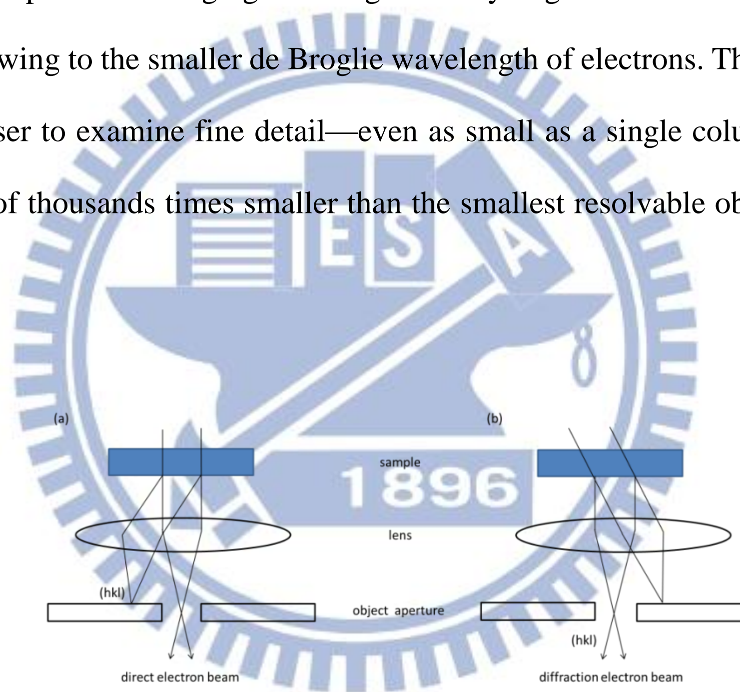

Fig 2. 10 Imaging methods of diffraction contrast: (a) bright field image and (b) dark field image.

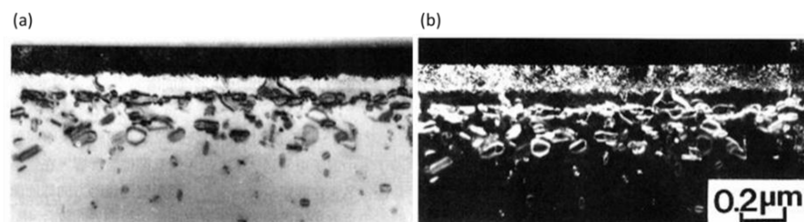

Fig 2. 11 (a) Bright field image and (b) dark field image of a BF^+ ion implantation sample.

2.2.4 Raman Spectrum

The Raman effect occurs when light impinges upon a molecule and interacts with the electron cloud and the bonds of that molecule. The momentum and energy maybe change when photon collide molecule. The former changes light propagation direction also called Rayleigh scattering. The latter is called Raman scattering when light energy changes after collision. Fig 2. 12 shows the principle of Raman Effect. [20] The relation between Raman shift (Δσ) and energy change (ΔE) is shown as equation (2-1):

$$\begin{aligned}\Delta\sigma &= \sigma \text{ (laser enegy)} - \sigma' \text{ (scattered light energy)} \\ &= \Delta E/hc \end{aligned} \qquad (2\text{-}1),$$

where h is Planck constant and c is light velocity.

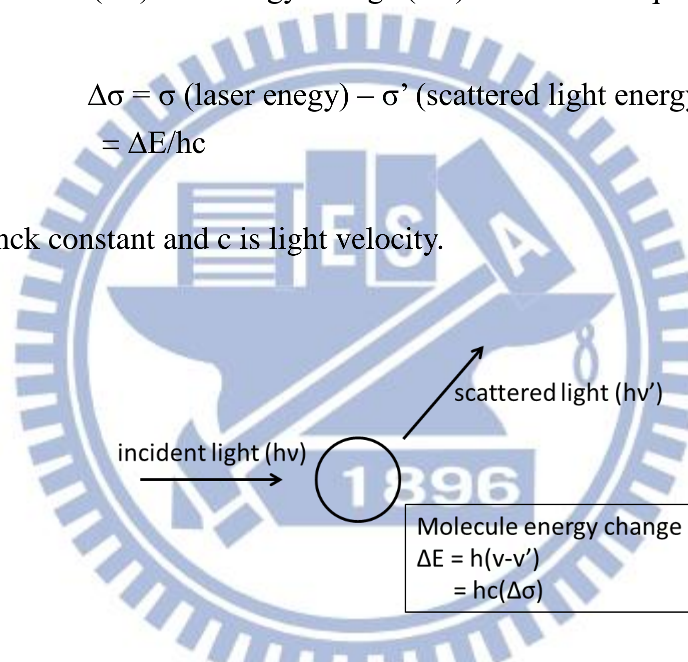

Fig 2. 12 Energy transfer of Raman effect.

For the spontaneous Raman effect, which is a form of light scattering, a photon excites the molecule from the ground state to a virtual energy state. When the molecule relaxes it to emit a photon, it returns to a different rotation or vibration state. The energy difference between the original state and the new state leads to a shift in the emitted photon's frequency away from the excitation wavelength. If the final vibrational state of the molecule is more energetic than the initial state, then the emitted photon will be shifted to a lower frequency in order to remain the balanced energy of the system. This

shift in frequency is designated as a Stokes shift. If the final vibrational state is less energetic than the initial state, then the emitted photon will be shifted to a higher frequency, and this is designated as an Anti-Stokes shift. Raman scattering is an example of inelastic scattering because of the energy transfer between the photons and the molecules during their interaction. Fig 2. 13 shows the diagram of Raman energy transition.

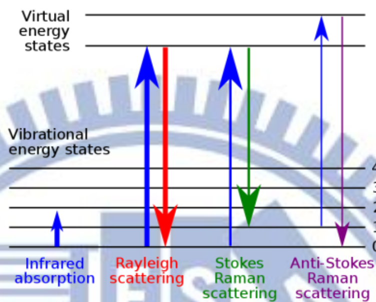

Fig 2. 13 Diagram of Raman energy transition.

In our experiment, the crystalline properties of Si QDs are confirmed by the Raman spectrum examined by a 488 nm diode-pumped solid-state (DPSS) laser (HOROBA, Lab RAM HR). The focused spot size is about 2 um in diameter, and the pumping power density is ~5 mW.

2.2.5 XRD Pattern

X-ray diffraction (XRD) is a non-destructively analytical techniques which can reveal the crystal structure, chemical composition, and physical properties of materials. These techniques are based on observing the diffraction intensity of an X-ray beam hitting a sample as a function of incident and diffracted angle, polarization, and wavelength or energy.

Crystals are regular arrays of atoms, and X-rays can be considered waves of electromagnetic radiation. Atoms scatter X-ray waves, primarily through the atoms' electrons. Just as an ocean wave striking a lighthouse produces secondary circular waves emanating from the lighthouse, so an X-ray striking an electron produces secondary spherical waves emanating from the electron. This phenomenon is known as elastic scattering, and the electron (or lighthouse) is known as the scatter. [20] A regular array of scatters produces a regular array of spherical waves. Although these waves cancel one another out in most directions through destructive interference, they add constructively in a few specific directions, determined by Bragg's law:

$$2d\sin\theta = n\lambda \qquad (2\text{-}2),$$

Here d is the spacing between diffracting planes, θ is the incident angle, n is any integer, and λ is the wavelength of the beam. Fig 2. 14 shows the diagram of Bragg's law. These specific directions appear as spots on the diffraction pattern called reflections. Thus, X-ray diffraction results from an electromagnetic wave (the X-ray) impinging on a regular array of scatters (the repeating arrangement of atoms within the crystal).

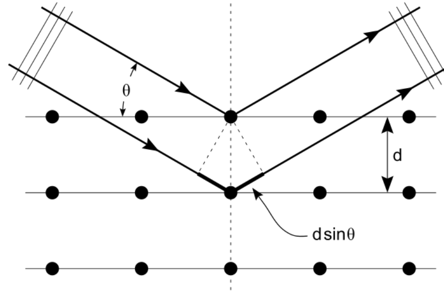

Fig 2. 14 Diagram of Bragg's diffraction.

Generally, grain size increases with decreasing FWHM. The larger grain size, the better electrical property is. The equation of calculating the grain size is shown as:

$$\text{Grain size} = 0.94 * \frac{\lambda}{d * \sin\theta} \quad (2\text{-}3),$$

here d is spacing between crystal plane.

For XRD measurement, the common methods are phase analysis (θ-2θ analysis) and grazing incident X-ray diffraction (GIXRD). Fig 2. 15 shows the diagram of θ-2θ analysis. The phase of bulk materials, thin films and powder samples is identified by the light source generates and receiver movement at different angles. For thin film samples, if the skin depth of X-ray was thicker than thin film, the signal of sample would be mainly from substrate. So, GIXD is used to measure thin film samples. Fig 2. 16 shows the diagram of grazing incident X-ray diffraction. The incident X-ray angle with thin film is fixed at very small degree and detector collects signal at different angles. This way can increase the interaction area between thin film and X-ray to enhance the signal of thin film. In our experiment, the X-ray diffraction patterns of ML sample is measured by GIXD with 2° incident angle and the system is Bede-D1 X-ray diffractometer (XRD) with Cu Kα radiation (λ = 1.5418 Å).

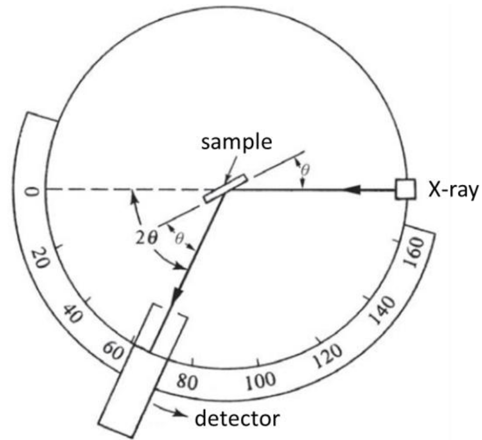

Fig 2. 15 Diagram of θ-2θ scanning method.

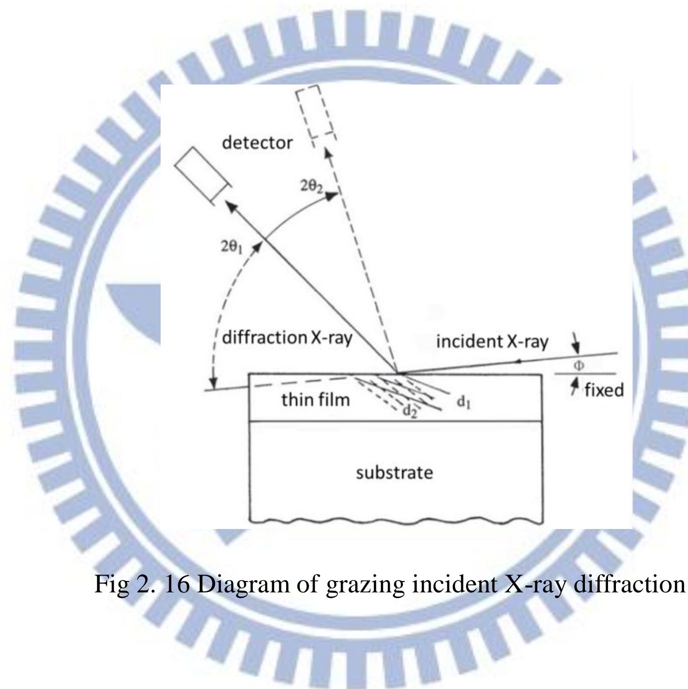

Fig 2. 16 Diagram of grazing incident X-ray diffraction.

2.2.6 UV-Vis-NIR Spectrum

Ultraviolet-visible-near infrared spectroscopy (UV-Vis-NIR) refers to absorption spectroscopy or reflectance spectroscopy in the UV-Vis-NIR region. The absorption or reflectance in the visible range directly affects the perceived color of the chemicals involved. The absorbance and reflectance are measured by UV-Vis-NIR and then absorption coefficient could be derived from $\alpha=A/d$, here A is the absorbance of materials and d is the film thickness. The optical characteristic of materials can be classified to direct and indirect bandgap. The equation of effective optical bandgap is shown below:

$$(\alpha h v)^{\gamma} = B(hv - E_{gopt}) \quad (2\text{-}4),$$

where h is Planck's constant, v is the frequency of the radiation, and B is the edge width parameter. The value of γ is dependent on the E_{gopt} behavior, such as $\gamma=2$ for direct $E_{g,opt}$ and $\gamma=1/2$ for indirect E_{gopt}. In our experiment, indirect bandgap is used to calculate optical bandgap. The reflection and transmittance spectra are measured by a Hitachi U-4100.

2.2.7 I-V Curve

The electrical properties of p-n junction between thin film and Si wafer can be understood by I-V characteristics. In addition, we can use I-V characteristics to estimate the vertical resistivity from the linear trend line in the high bias region. We can calculate the resistivity by combining the resistance as equation (2-5):

$$R = \rho \frac{L}{A} = \rho \frac{L}{Wt} \quad (2\text{-}5),$$

where ρ is the resistivity, A is the cross-sectional area, and L is the length. The cross-sectional area can be split into the width W and the thickness t. In our experiment, the I-V curves are measured by using a E5270B 8-slot precision measurement mainframe (Agilent Technologies), and a halogen lamp with power density of ~20 mW/cm^2 is used for photo-response measurements.

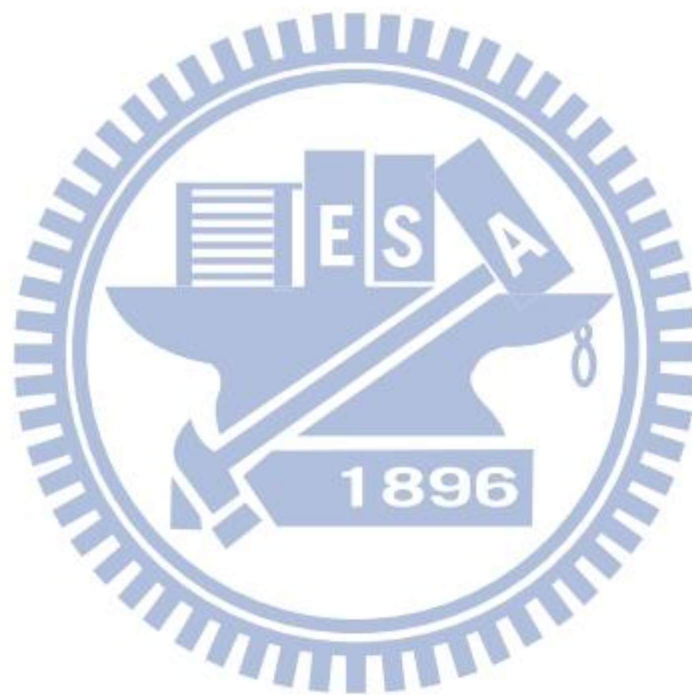

Chapter 3 Results and Discussions

3.1 [ZnO/Si] Multilayer Thin Films

The annealing temperature is important for the crystallization of Si QDs and ZnO matrix, therefore, the [ZnO/Si] ML thin films were annealed from 300 to 1000 ^{o}C for 30 minutes. The crystalline, electrical, and optical properties of the [ZnO/Si] ML thin films under different annealing temperature are discussed here.

3.1.1 Structural Properties

The surface morphologic images of the as-deposited ZnO (5 nm) and ZnO(5 nm)/Si(3 nm) thin films by AFM are shown in Fig 3. 1, the self-assemble Si nano-clusters are clearly formed on ZnO thin-layer. To further confirm the formation of Si nano-clusters, the high resolution transmission electron microscopy (HRTEM) images are also examined, as shown in Fig 3. 2. It indicates the clear ML structure and the self-assembled a-Si nano-clusters with size range from 2 to 5 nm. Hence, we demonstrate that the self-assembled a-Si nano-clusters can be formed by a [ZnO/Si] ML deposition structure with a high Si sputtering power.

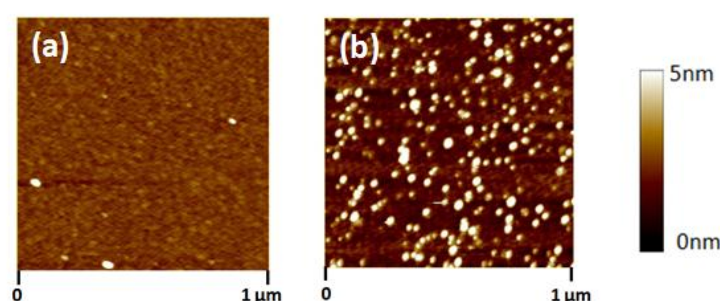

Fig 3. 1 Surface morphologic images of the as-deposited ZnO (5 nm) and ZnO(5 nm)/Si(3 nm) thin films by AFM.

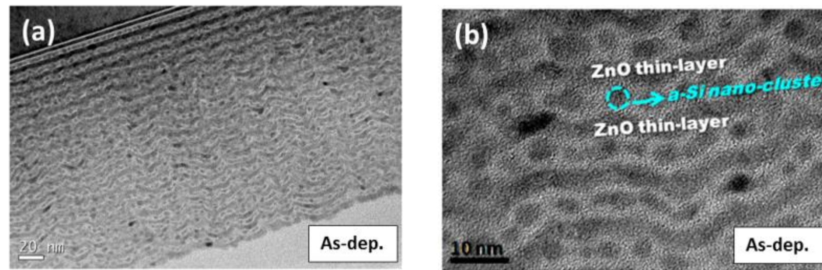

Fig 3. 2 (a) Low magnification and (b) high magnification HRTEM images of the as-deposited [ZnO/Si] ML thin films.

3.1.2 Crystalline Properties of Si QDs

From literatures, Raman spectrum of the Si QD thin films can be decomposed into three components with peaks located at ~480, 500~510, and 510~520 cm^{-1}, which are contributed from the transverse optical (TO) modes of Si-Si vibrations in the amorphous (a-Si), intermediate (i-Si), and nano-crystalline (nc-Si) phases of Si respectively. [21] Hence, the Raman spectra of the annealed samples under different annealing temperature are performed to understand the variation of the crystalline properties of Si QDs, as shown in Fig 3. 3, the nc-Si signals are clearly observed in samples annealed at higher than 600 ^{o}C. The curve-fitting result of sample F1000 is also confirmed, as shown in Fig 3. 4, it shows the well matched result with the measured data.

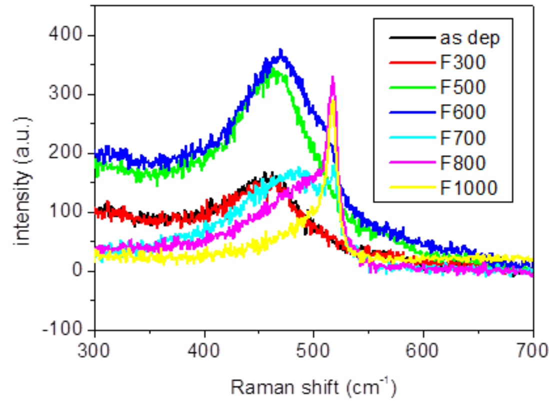

Fig 3. 3 Raman spectra of the annealed ML thin films under different annealing temperature for 30 minutes.

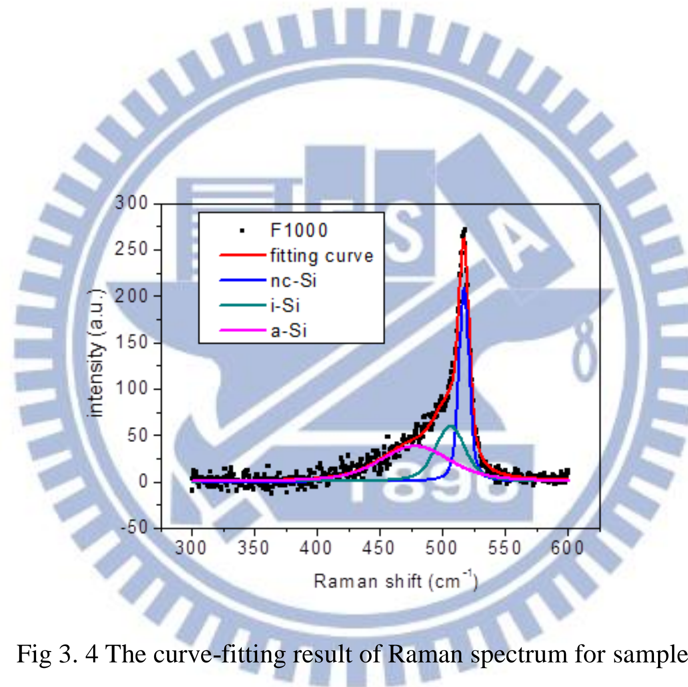

Fig 3. 4 The curve-fitting result of Raman spectrum for sample F1000.

The parameters of the curve-fitting results from Raman spectra are shown in Table 3. 1, the corresponding plots are shown in Fig 3. 5. Here the Si crystallinity (C_{Si}) is estimated by equation (3-1) as below:

$$\text{Si Crystallinity (\%)} = \frac{I_{nc}+I_{i}}{I_{nc}+I_{i}+I_{a}} \times 100\% \qquad (3\text{-}1),$$

where I_{nc}, I_{i} and I_{a} are the integrated intensities of a-Si, i-Si, and nc-Si peaks. With increasing the annealing temperature, the increased C_{Si} and integrated intensity and the reduced FWHM values for the nc-Si signals represent the formation of the better

crystalline quality of Si QDs.

Table 3. 1 Parameters for the crystalline properties of Si QDs under different annealing temperature.

Sample ID	Peak Position of nc-Si (cm^{-1})	FWHM (cm^{-1})	Integrated Intensity (a.u.)	Crystallinity (%)
As-dep	/	/	0	0
F300	/	/	0	0
F500	/	/	0	0
F600	514	14.2	522.3	7.4%
F700	518	10.3	849.8	40.5%
F800	517	9.3	1928.1	50.3%
F1000	517	9.7	2522.8	60.6%

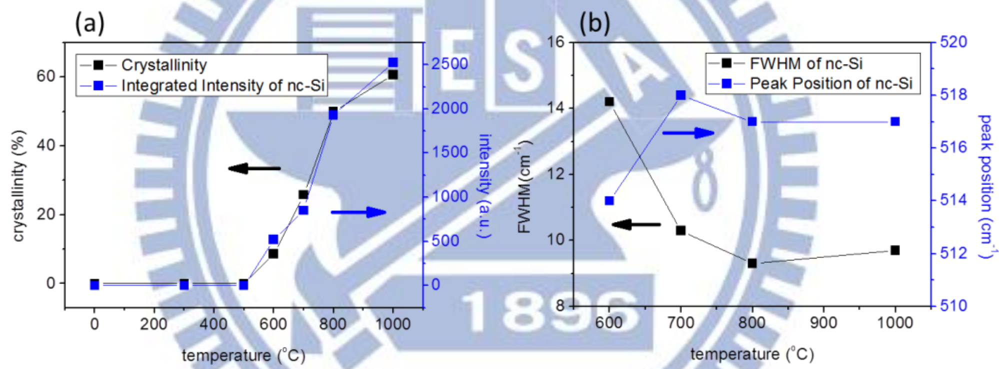

Fig 3. 5 (a) Crystallinity and integrated intensity and (b) FWHM and peak position for the nc-Si QDs from Raman spectra.

3.1.3 Crystalline Properties of ZnO Matrix

The crystalline property of ZnO matrix has strong influences on the optical and electrical properties of the ZnO thin films. [22] Fig 3. 6 shows the XRD patterns of the annealed ML thin films, the c-axis (002) preferred orientation of ZnO matrix is clearly observed. Inset of Fig 3. 6 shows the large range XRD scan from 20 to 60° for sample F300, there are no other crystallization signals observed. All annealed samples show the same results.

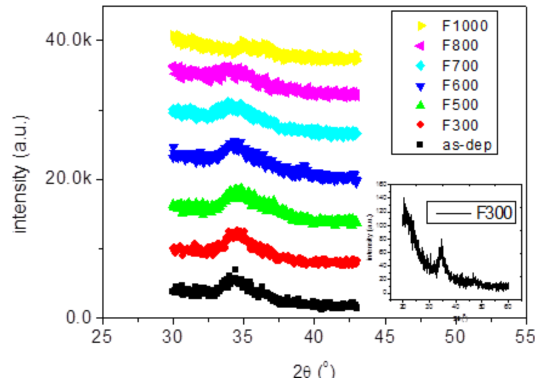

Fig 3. 6 XRD patterns of the annealed ML samples. Inset shows the XRD pattern from 20 to 60° for sample F300.

The XRD pattern of ZnO bulk locates at ~34.4^o and the d-spacing value is about 2.60 Å . [23] The stress in ZnO thin film will affect characteristic of ZnO thin film.[24] In our experiment, the crystalline signals of ZnO(002) have to be decomposed into two components contributed from the normal and stressed ZnO crystals with peaks located at ~34.4^o and 35.5~36.7^o individually. The curve-fitting results from XRD patterns are shown in Table 3. 2, and Fig 3. 7 shows the integrated intensity of the normal, stressed, and total ZnO(002) crystals. Sample F500 has the largest residual film stress since it shows the highest stressed intensity, it may be caused by the increased amounts of ZnO(002) or a-Si from the phase separation of the silicon-rich oxide ($SiO_x \rightarrow Si + SiO_2$). In addition, the total ZnO(002) intensities of the samples annealed over 500°C decrease with annealing temperature possibly due to the restriction from the phase transformation of Si QDs from a- to c-Si phases.

Table 3. 2 Crystalline properties of ZnO(002) for the annealed samples.

	peak	FWHM	integrate area (%)	d(hkl) (A)
as-dep	34.5	2.0	83.2	2.60
	36.5	**1.2**	**16.8**	**2.46**
F300	34.5	2.0	82.4	2.60
	36.6	**1.6**	**17.6**	**2.45**
F500	34.5	2.1	63.9	2.60
	36.7	**2.3**	**36.1**	**2.45**
F600	34.4	1.8	74.6	2.61
	36.3	**1.6**	**25.4**	**2.47**
F700	34.3	2.3	79.6	2.61
	36.3	**1.7**	**20.4**	**2.47**
F800	34.4	2.8	96.5	2.61
	35.9	**1.6**	**3.5**	**2.50**
F1000	35.0	0.6	27.7	2.56
	36.3	**1.5**	**72.3**	**2.47**

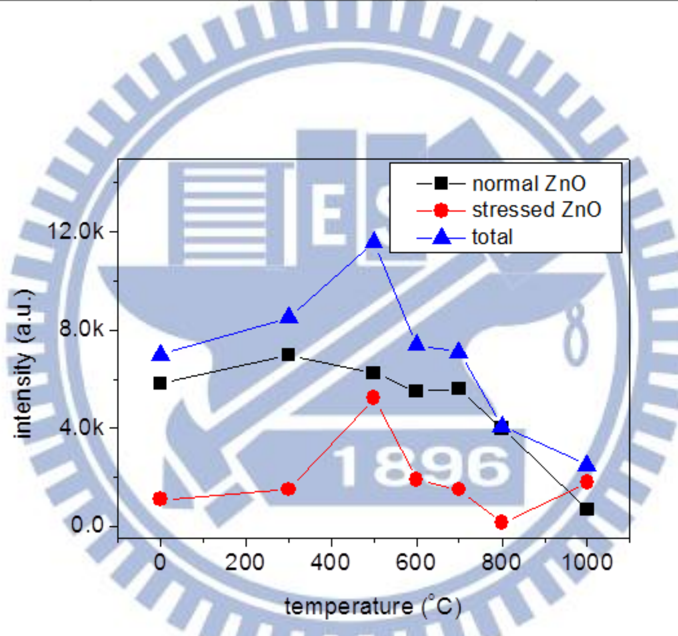

Fig 3. 7 Integrated intensities of the normal, stressed, and total ZnO(002) for the annealed samples.

3.1.4 Film Stress

Fig 3. 8 shows the SEM images of samples F500 and F1000 for 30 minutes, the bended film is observed in sample F1000. Fig 3. 9 also shows the bending area ratio and bending density of the annealed samples. It indicates the film bending problem will occur while the annealing temperature is >500°C, and the bending density and

ratio clearly increase with increasing the annealing temperature. Comparing with the crystalline properties of the Si QDs from Raman spectra, nc-Si signals are observed from 600°C and also increased with increasing the annealing temperature. The crystal structure of ZnO is wurtzite and the crystal structure of Si is face-centered cubic crystal structure. [25] Hence, it means the film bending problem comes from the over-large film stress mainly due to the phase transformation of Si QDs from a- to c-Si phases during annealing.

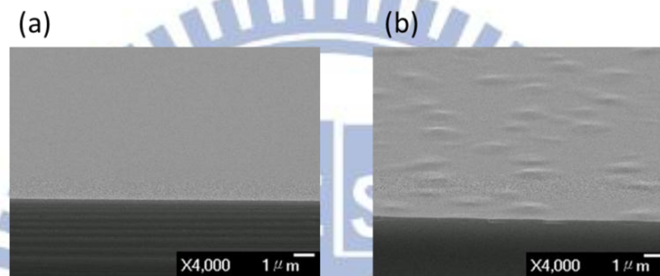

Fig 3. 8 SEM images of the samples annealed at (a) 500°C and (b) 1000 °C for 30min.

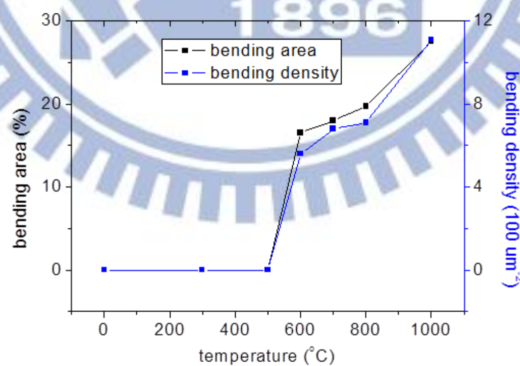

Fig 3. 9 Ratio of bending area and bending density of the annealed samples.

3.1.5 Optical Properties

Fig 3. 10 shows the absorbance (A) and transmittance (T) of the annealed

samples. In the long-wavelength range, the samples annealed at ≦500 °C show the low T and high A due to more deficiencies from a-Si QDs, the samples annealed at >600 °C show the low A and high T owing to the reduced deficiencies from the obvious nc-Si QDs formation. In addition, the highest absorbance of the sample annealed at 500 °C is observed, it means that the stressed ZnO(002) leads to a larger defects formation than normal ZnO(002). The low A and high T observed in samples annealed at >600 °C are the good results for tandem solar cell application because the upper cell of tandem solar cells needs to avoid the obvious light absorption in the long-wavelength.

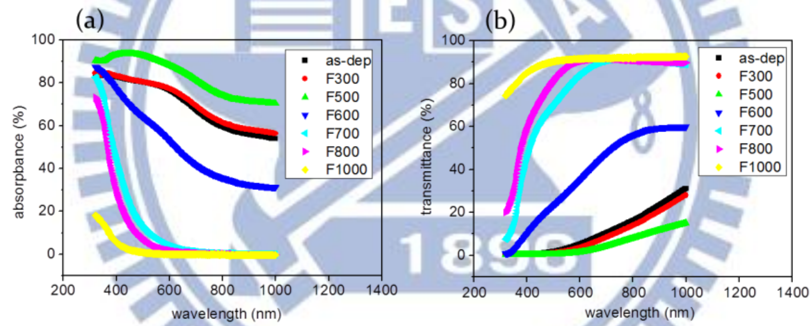

Fig 3. 10 (a) Absorbance and (b) transmittance of the annealed samples.

3.1.6 Electrical Properties

The band diagrams of p-type Si wafer and n-type ZnO thin films and the corresponding I-V curve are shown in Fig 3. 11. Here the Fermi level of Si wafer ($E_{f(Si)}$) from its conduction band is ~0.76 eV due to the doping concentration of ~10^{16} cm^{-3} used. Besides, according to literatures, we know the conduction band of Si is close to that of ZnO. [26] Hence, the combination of these two materials can form the

hetero-junction as a diode, and the turn-on voltage (V_t) is mainly influenced by the Fermi level difference between both materials. In addition, since the Si QDs are embedded in the ZnO matrix, it can be expected that the crystalline quality of Si QDs may affect the effective Fermi level of thin films.

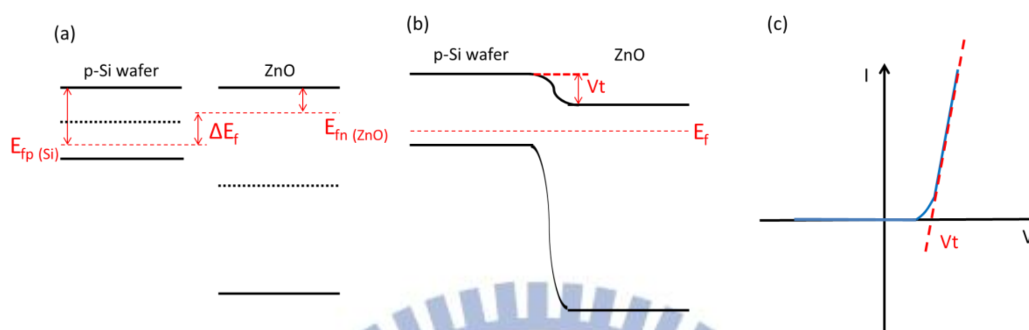

Fig 3. 11 Band diagrams of p-type Si wafer and n-type ZnO material (a) before and (b) after combination and (c) the I-V curve of the hetero-junction cell.

The dark I-V curves of the annealed samples are shown in Fig 3. 12. The samples annealed at <500 ^{o}C shows the good I-V properties, however, the current orders are decreased in the samples annealed at >500 ^{o}C because of the film bending problem. The film bending regions will lead to the formations of open-circuit and interface defect and limit the electrical transportation properties. Fig 3. 13 (a) shows the V_t of the annealed samples from the dark I-V curves. To compare with the above results, the increased V_t (a larger build-in electric field) from 600 ^{o}C is possibly resulted from the improved crystalline quality of Si QDs or the film bending problem with increasing the annealing temperature. Fig 3. 13 (b) shows the vertical resistivity from the dark I-V curves, the samples annealed at ≦700 ^{o}C has the good resistivity with <10^5 Ω-cm, which are obviously lower than that of un-doped Si QDs using SiO_2 matrix for ~10^8 Ω-cm. [27] The resistivity of samples annealed at ≧800 ^{o}C is largely increased due to the serious film bending problem.

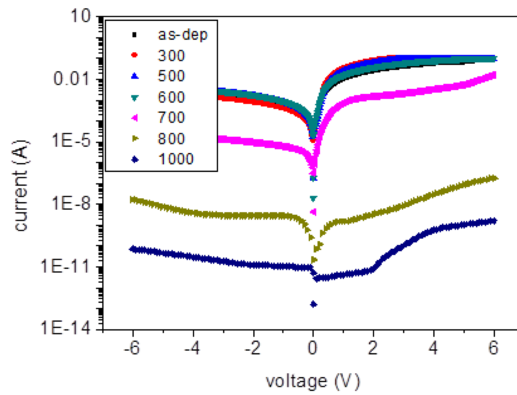

Fig 3. 12 Dark I-V curves of the annealed samples.

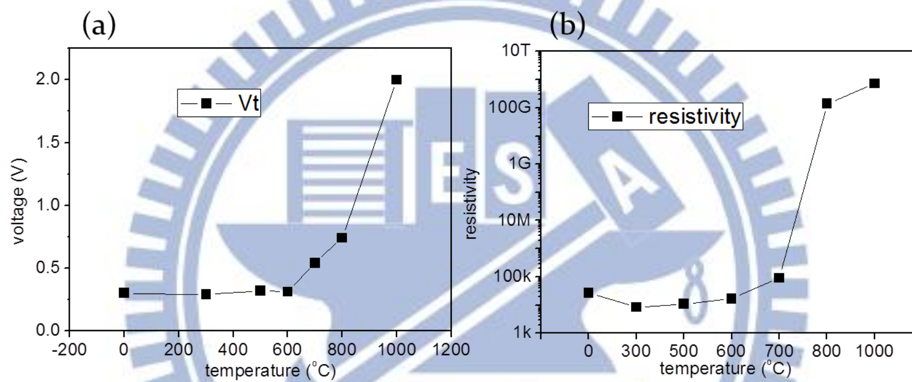

Fig 3. 13 (a) Turn-on voltage and (b) vertical resistivity of the annealed samples.

Fig 3. 14 shows the light I-V curves of the annealed samples, here the result for sample annealed at 1000 °C couldn't be shown due to a charging effect. The corresponding open circuit voltage (V_{OC}) and short circuit current (I_{SC}) are also shown in Fig 3. 15. In Fig 3. 15 (a), the trend of V_{OC} is similar with V_t while increasing the annealing temperature, hence, it means the increased V_t with increasing the annealing temperature from 600 to 800 °C is mainly contributed from the increased crystallinity of Si QDs. The improved crystalline quality of Si QDs will lead to a higher effective $E_{f(ZnO)}$ and form a larger build-in electric field. In Fig 3. 15 (b), the I_{SC} of samples annealed at $<$500 °C is slightly decreased with increasing the annealing temperature,

it may be caused by the increased residual film stress. When the annealing temperature is higher than 500 °C, the I_{SC} obviously increases with increasing the annealing temperature and achieve the highest value at 700 °C due to the c-Si QDs formation. The I_{SC} of sample annealed at 800 °C largely reduced by the high resistivity owing to the serious film bending problem. Hence, the sample annealed at 700 °C has the better electro-optical properties for PV application.

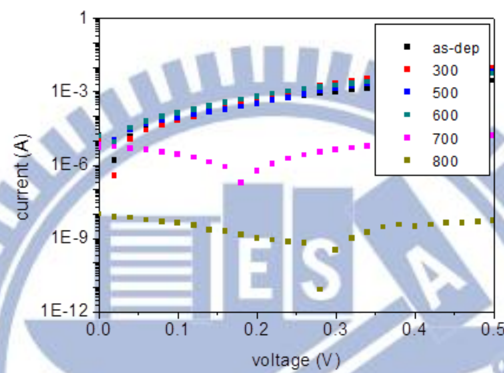

Fig 3. 14 Light I-V curves of the annealed samples.

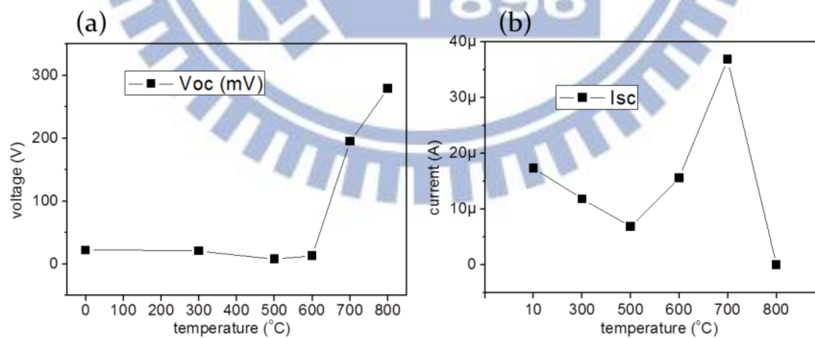

Fig 3. 15 (a) Open circuit voltage and (b) short circuit current of the annealed samples.

3.2 a-Si QDs embedded ZnO thin films

As the discussions in section 3.1, 500 ^oC is a critical annealing temperature without film bending problem observed. Although the I_{SC} and V_{OC} are reduced from the high residual film stress, but it has the highest crystalline intensity of ZnO(002) and low resistivity. Therefore, the sample annealed at 500 ^oC has the potential for further improvement on PV properties for the a-Si QD embedded ZnO thin films by optimizing the annealing conditions. In this section, the properties of a-Si QD thin films with and without H_2 annealing will be discussed here.

3.2.1 Crystalline Properties

Fig 3. 16 (a) shows the Raman spectra of samples annealed at 500 ^oC for 30 minutes, 1 hour, and 2 hours. Similar a-Si signals are observed in these three samples. The XRD patterns for the crystalline properties of ZnO matrix are shown in Fig 3. 16 (b), the ZnO(002) peaks can be well-fitted by the normal and stressed ZnO components. Table 3. 3 show the curve-fitting results for the normalized integrated intensity. The total ZnO(002) intensity is increased by increasing the annealing time, and the stressed ZnO(002) intensity is reduced while the annealing time is longer than 1 hour. Hence, the sample annealed at 500 ^oC for 2 hours has the better crystalline properties of ZnO(002), and it indicates that the crystalline quality of ZnO matrix can be improved by increasing the annealing time at 500 ^oC.

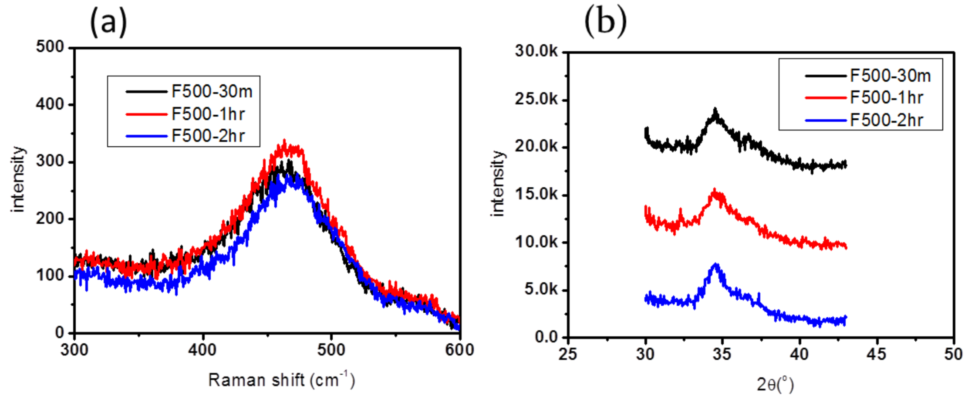

Fig 3. 16 (a) Raman spectra and (b) XRD patterns of the samples annealed at 500 °C under different annealing time.

Table 3. 3 Curve-fitting results for the crystalline properties of ZnO matrix of the samples annealed at 500 °C under different annealing time.

Sample ID	Normalized Integrated Intensity (a. u.)		
	Normal ZnO(002)	Stressed ZnO(002)	Total
F500-30m	5.8E+3	5.8E+3	11.6E+3
F500-1hr	7.2E+3	4.1E+3	11.3E+3
F500-2hr	8.1E+3	4.6E+3	12.7E+3

3.2.2 Electrical Properties

Fig 3. 17 shows the dark and light I-V curves of the samples annealed at 500 °C for 30 minutes, 1 hour and 2 hours, and the corresponding electrical parameters are shown in Table 3. 4. The V_t, rectification, V_{OC}, and I_{SC} are improved by increasing the annealing time, which are matched with the result of the total crystalline intensity of ZnO(002). However, the ideal factors seems to be affected by the stressed ZnO(002) intensity. The ideal factor larger than 2 is also observed in the Si QD thin films by other group's work, the cause had been demonstrated due to the trapping effect from defects. [28] Hence, the defect density in the a-Si QD embedded ZnO thin film is

dominated by the stressed ZnO(002) intensity.

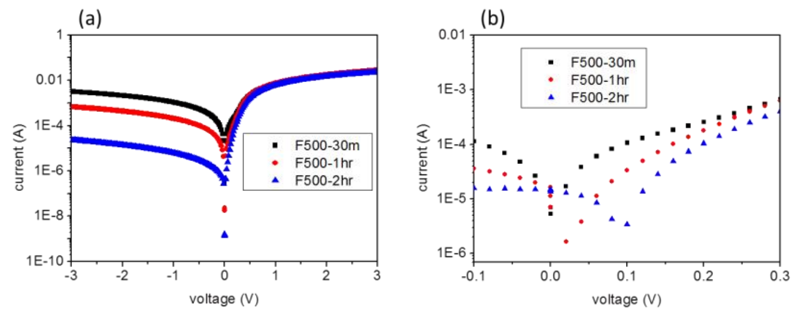

Fig 3. 17 (a) Dark and (b) light I-V curves of the samples annealed at 500 ^{o}C under different annealing time.

Table 3. 4 Parameters from I-V curves of the samples annealed at 500 ^{o}C under different annealing time.

Sample ID	Dark I-V				Light I-V	
	Vertical resistivity (Ω*cm)	Rectification	Vt (V)	Ideal factor	Voc (mV)	Isc (A)
F500-30m	4.1E+4	8.6E0	0.26	5.3	8	6.9E-06
F500-1hr	4.1E+4	4.1E+1	0.28	3.3	45	1.1E-05
F500-2hr	4.3E+4	9.8E+2	0.32	3.7	109	1.4E-05

3.3 a-Si QDs embedded ZnO thin films with H_2 annealing

In the Si QDs thin film references, the defects at the interface of Si QDs and SRO can be eliminated by H_2 annealing. [29] In the ZnO thin film references, the defects can be eliminated by H_2 annealing and H atom can be a better donor. [30, 31] Therefore, we expect defects and quality of thin film can be improved after H_2 annealing.

The sample annealed at 500 ^oC for 2 hours is chosen to be annealed in H_2 environment for 1 hour and the annealing temperature is tried from 300 to 500 ^oC. The sample annealed at 500 ^oC in H_2 shows the better PV properties; hence, here it is compared with the reference sample annealed in N_2 at 500 ^oC for 1 hour more.

3.3.1 Crystalline and Optical Properties

Fig 3. 18 (a) shows the Raman spectra of the annealed samples after N_2 and H_2 annealing, both samples show the similar a-Si signals. Fig 3. 18 (b) shows the XRD patterns. The normalized integrated intensity of stressed ZnO(002) is clearly reduced in H_2 annealing (~3.4×10^2 a. u.) than that in N_2 annealing (~2.7×10^3 a. u.). It means the crystalline quality of ZnO matrix can be efficiently improved by using a H_2 annealing process.

The absorbance and transmittance of the annealed samples after N_2 and H_2 annealing are shown in Fig 3. 19. The absorbance and transmittance are obviously improved in the long-wavelength range by H_2 annealing due to the better crystalline quality of ZnO matrix.

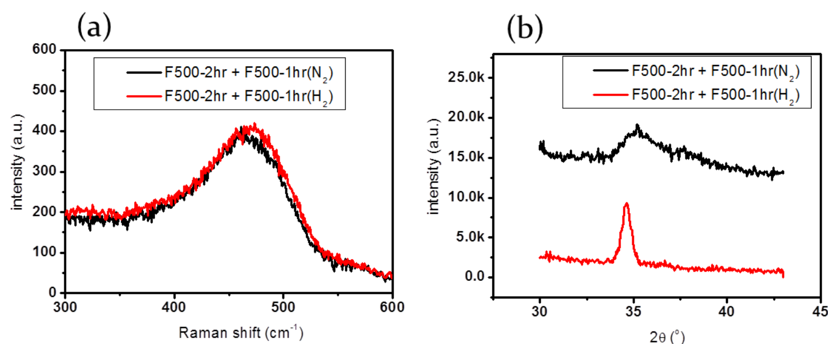

Fig 3. 18 (a) Raman spectra and (b) XRD patterns of the annealed samples after N_2 and H_2 annealing.

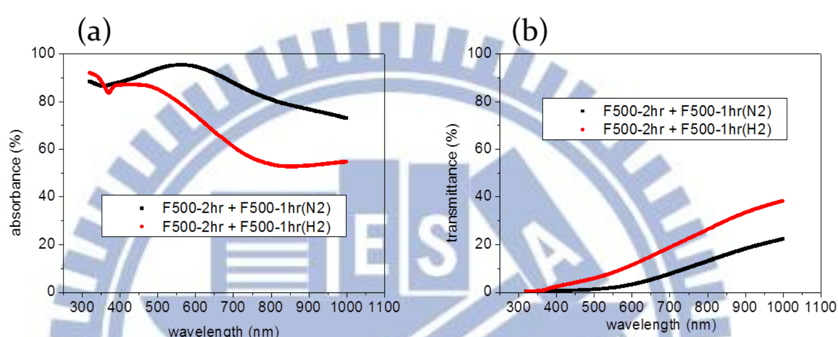

Fig 3. 19 (a) Absorbance and (b) transmittance of the annealed samples after N_2 and H_2 annealing.

3.3.2 Electrical Properties

Fig 3. 20 shows the dark and light I-V curves of the annealed samples after N_2 and H_2 annealing, and the corresponding parameters are shown in Table 3. 5. The ideal factor of the sample annealed in H_2 (~3.0) is lower than that in N_2 (~4.5), which is meaning the decreased defect density. From XRD results, it indicates that the decreased defect density is contributed from the reduced intensity of stressed ZnO(002) by H_2 annealing. In addition, the photo-response properties including the V_{OC} and I_{SC} are also clearly enhanced by H_2 annealing. Therefore, we demonstrate that the optical properties and photo-response properties of the a-Si QD embedded

ZnO thin films can be efficiently improved by H_2 annealing, and more enhancements can be expected by optimizing the H_2 annealing conditions.

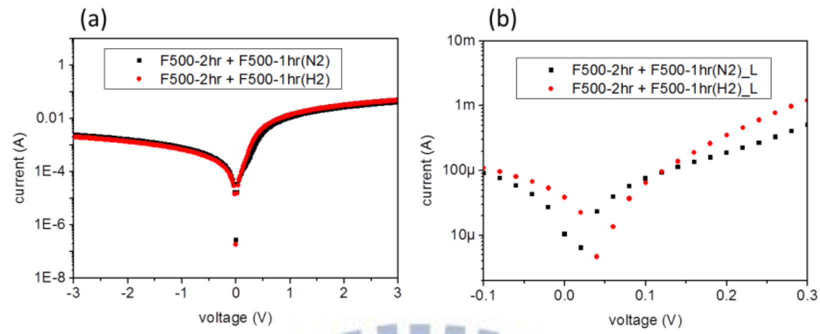

Fig 3. 20 (a) Dark and (b) light I-V curves of the annealed samples after N_2 and H_2 annealing.

Table 3. 5 Parameters from I-V curves of the annealed samples after N_2 and H_2 annealing.

Sample ID	Vertical Resistivity (Ω*cm)	Rectification	Vt (V)	Ideal factor	Voc (mV)	Isc (A)
F500-2hr + F500-1hr(N_2)	2.3E+4	1.7E+1	0.31	4.5	12	1.0E-5
F500-2hr + F500-1hr(H_2)	2.1E+4	2.4E+1	0.24	3.0	47	3.9E-5

3.4 c-Si QDs embedded ZnO thin films

In section 3.1, the better PV properties of the c-Si QD embedded ZnO thin films is observed at 700 ^{o}C. Hence, in this section, the properties of the c-Si QD embedded ZnO thin films are discussed and optimized by tuning the annealing time.

3.4.1 Crystalline Properties

Fig 3. 21 shows the Raman spectra and XRD patterns of the samples annealed at 700 oC for 30 minutes, 1 hour, and 2 hours, the corresponding parameters are shown in Table 3. 6. The nc-Si signal is clearly observed in these three samples, and it shows the higher Si crystallinity as increasing the annealing time. The stressed ZnO(002) intensity is reduced when the annealing time is longer than 30 minutes, however, the total ZnO(002) intensity is also decreased at the same time. It indicates that the longer annealing time at 700 ^{o}C possibly decrease the crystalline quality of ZnO matrix for the c-Si QDs embedded ZnO thin films. Fig 3. 22 shows the film bending density of the samples annealed at 700 ^{o}C under different annealing time, it indicates the film bending density doesn't increase while increasing the annealing time at 700 ^{o}C.

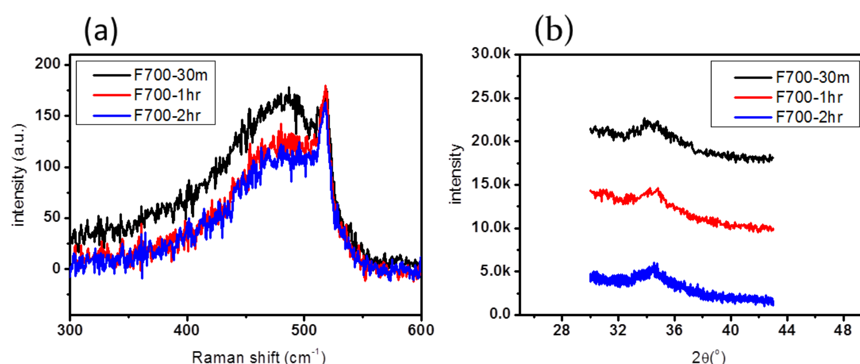

Fig 3. 21 (a) Raman spectra and (b) XRD patterns of the samples annealed at 700 ^{o}C under different annealing time.

Table 3. 6 Curve-fitting results from XRD patterns of the samples annealed at 700 °C under different annealing time.

sample ID	Raman for nc-Si			XRD for ZnO(002)		
	Peak Position (cm^{-1})	FWHM (cm^{-1})	Crystallinity (%)	Normal ZnO(002)	Stressed ZnO(002)	Total
F700-30m	518.1	10.5	19.9	5.6E+3	1.4E+3	7.0E+3
F700-1hr	517.9	7.4	23.9	4.7E+3	0.6E+3	5.3E+3
F700-2hr	517.5	7.8	25.4	5.1E+3	0.8E+3	5.9E+3

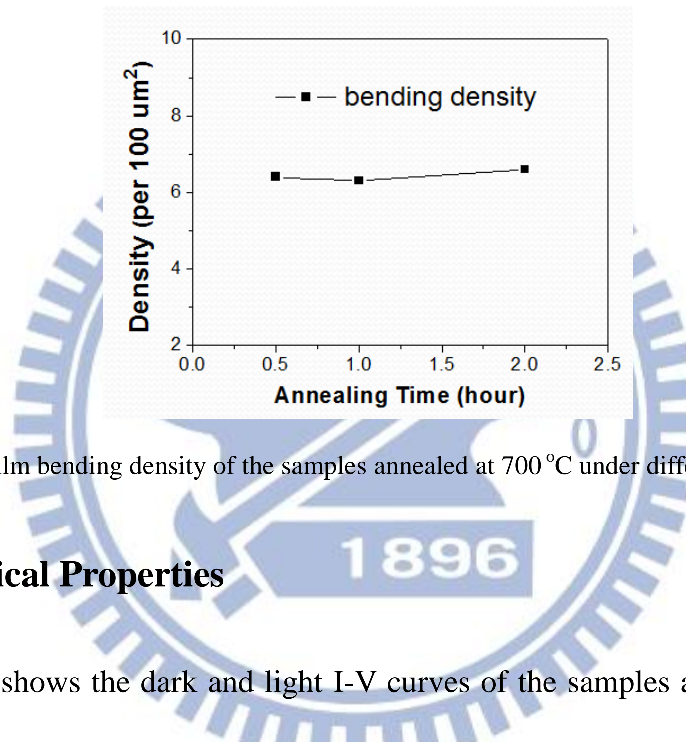

Fig 3. 22 Film bending density of the samples annealed at 700 °C under different annealing time.

3.4.2 Electrical Properties

Fig 3. 23 shows the dark and light I-V curves of the samples annealed at 700 °C under different annealing time, and the corresponding parameters are shown in Table 3. 7. Here the ideal factors are larger than those of a-Si QD thin films because of the film bending problem in the c-Si QD thin films, however, it's also clearly affected by the stressed ZnO intensity. As increasing the annealing time, the V_t and V_{OC} simultaneously increase may due to the higher Si crystallinity formation, however, it also lead to the higher resistivity. Hence, it indicates the longer annealing time could lead to the negative result such as the decreased I_{SC} from 1 to 2 hours.

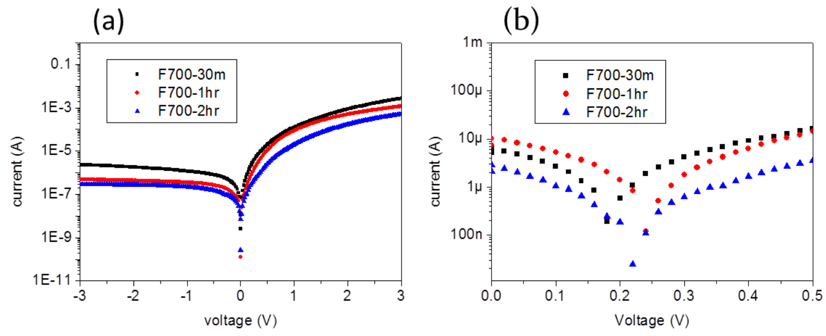

Fig 3. 23 (a) Dark and (b) light I-V curves of the samples annealed at 700 °C under different annealing time.

Table 3. 7 Parameters from I-V curves of the annealed samples at 700 °C under different annealing time.

	Vertical resistivity (Ω*cm)	Rectification	Vt (V)	Ideal factor	Voc (mV)	Isc (A)
F700-30m	9.1E+4	1.2E+3	0.54	12.3	204	6.9E-06
F700-1hr	5.5E+5	2.4E+3	0.61	10.6	223	1.0E-05
F700-2hr	5.9E+5	1.8E+3	0.65	10.8	244	2.9E-06

3.5 c-Si QDs embedded ZnO thin films with H_2 annealing

In this section, the crystalline, optical, and electrical properties of the c-Si QDs embedded ZnO thin films after H_2 annealing are discussed.

3.5.1 Crystalline and Optical Properties

Fig 3. 24 shows the Raman spectra and XRD patterns of the annealed samples after N_2 and H_2 annealing, and the corresponding curve-fitting results are shown in Table 3. 8. The crystalline properties of Si QDs are similar by N_2 and H_2 annealing such as the crystallinity and FWHM values. However, the total intensity of ZnO(002) is increased by H_2 annealing, it means the H2 annealing process can also improve the crystalline properties of ZnO matrix for the c-Si QDs embedded ZnO thin films.

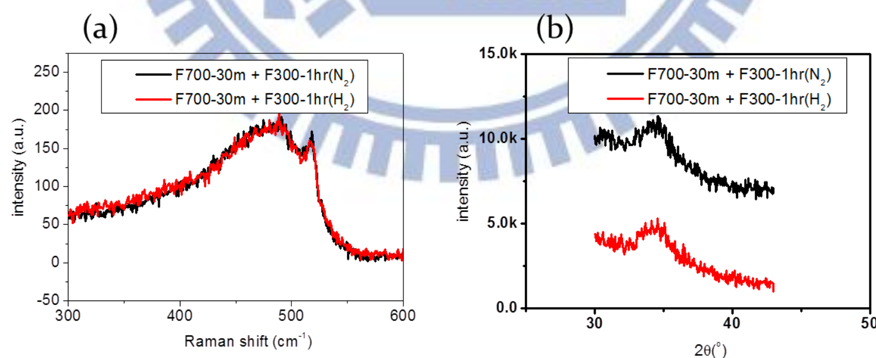

Fig 3. 24 (a) Raman spectra and (b) XRD patterns of the annealed samples after N_2 and H_2 annealing.

Table 3. 8 Curve-fitting results from Raman spectra and XRD patterns of the annealed samples after N_2 and H_2 annealing.

Sample ID	Raman for nc-Si			XRD for ZnO(002)		
	Peak Position (cm^{-1})	FWHM (cm^{-1})	Crystallinity (%)	Normal ZnO(002)	Stressed ZnO(002)	Total
F700-30m + F300-1hr(N_2)	517.9	10.2	18.2	5.6E+3	0.4E+3	6.0E+3
F700-30m + F300-1hr(H_2)	517.9	10.6	18.0	8.8E+3	0.8E+3	9.6E+3

3.5.2 Electrical Properties

Fig 3. 25 shows the dark and light I-V curves of the samples after N_2 and H_2 annealing, and the corresponding parameters are shown in Table 3. 9. The V_t, resistivity, and rectification are obviously enhanced because of the improved quality of ZnO matrix after H_2 annealing. Besides, the ideal factor is also clearly reduced after H_2 annealing, which is meaning the decreased defect density. Hence, the Si QD thin films after H_2 annealing show the better photo-response properties due to the improvement of crystalline properties of ZnO matrix.

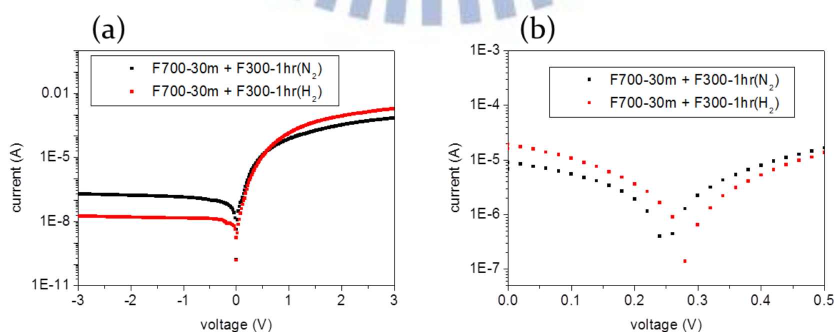

Fig 3. 25 (a) Dark and (b) light I-V curves of the samples after N_2 and H_2 annealing.

Table 3. 9 Parameters from I-V curves of the annealed samples after N_2 and H_2 annealing.

Sample ID	Vt (V)	Resistivity (Ω*cm)	n	Rectification	Voc (mV)	Isc (A)
F700-30m + F300(N_2)	0.54	1.4E+5	12.8	3.6E+3	249	9.0E-6
F700-30m + F300(H_2)	0.64	5.6E+4	9.0	1.1E+5	289	1.9E-5

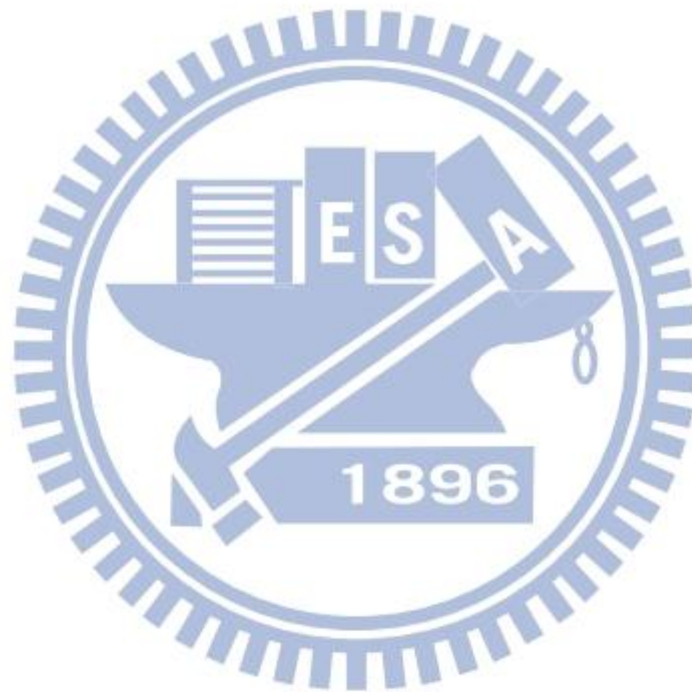

Chapter 4 Conclusion

The Si QD embedded ZnO thin films had been successfully fabricated by using a [ZnO/Si] ML structure. The resistivity of the Si QD embedded ZnO thin films annealed at <700 ^{o}C is obviously lower than that using a SiO_2 matrix. When the annealing temperature is <500 ^{o}C, no crystalline Si signals are observed. The a-Si QD embedded ZnO thin films annealed for 30 minutes show the good I_{SC} but low V_{OC}. When the annealing temperature is >600 ^{o}C, the crystalline Si signals can be observed. The c-Si QD embedded ZnO thin films show the good optical properties with the high-T and low-A in the long-wavelength range. At the annealing temperature of 700 ^{o}C for 30 minutes, the good I_{SC} and V_{OC} are simultaneously observed. However, the film bending problem is also examined in the c-Si QD embedded ZnO thin films due to the phase transformation of a- to c-Si QDs embedded in c-ZnO matrix.

For the a-Si QD embedded ZnO thin film, the residual film stress is reduced by increasing the annealing temperature or using a H_2 annealing process. The reduced film stress can lead to the better optical properties and the lower defect density and improve the PV properties. For the c-Si QD embedded ZnO thin films, the increased annealing temperature reduces the residual film stress and slightly increases the Si crystallinity, however, it also decreases the crystalline intensity of ZnO matrix. That result makes the optimal annealing time for better PV properties is at 1 hour not 2 hours. More improvements of PV properties are also observed by using a H_2 annealing process due to the enhanced crystalline intensity of ZnO matrix.

In the future, more enhancements on the PV properties of the Si QD thin films can be expected by using the ZnO matrix material after resolving the largely residual film stress.

Reference

[1] M. Wiemer, V. Sabnis, and H. Yuen, "43.5% Efficient Lattice Matched Solar Cells," *High and Low Concentrator Systems for Solar Electric Applications Vi,* vol. 8108, 2011.

[2] L. Y. Han, A. Islam, H. Chen, C. Malapaka, B. Chiranjeevi, S. F. Zhang, X. D. Yang, and M. Yanagida, "High-efficiency dye-sensitized solar cell with a novel co-adsorbent," *Energy & Environmental Science,* vol. 5, pp. 6057-6060, 2012.

[3] S. H. Hong, Y. S. Kim, W. Lee, Y. H. Kim, J. Y. Song, J. S. Jang, J. H. Park, S. H. Choi, and K. J. Kim, "Active doping of B in silicon nanostructures and development of a Si quantum dot solar cell," *Nanotechnology,* vol. 22, 2011.

[4] S. Y. Lien, Y. C. Chang, Y. S. Cho, Y. Y. Chang, and S. J. Lee, "Deposition and Characterization of High-Efficiency Silicon Thin-Film Solar Cells by HF-PECVD and OES Technology," *IEEE Transactions on Electron Devices,* vol. 59, pp. 1245-1254, 2012.

[5] M. A. Green, "Third generation photovoltaics: Ultra-high conversion efficiency at low cost," *Progress in Photovoltaics,* vol. 9, pp. 123-135, 2001.

[6] W. W. Shockley, "Elective Neck Dissection for Melanoma - the Great Debate," *Southern Medical Journal,* vol. 79, pp. 37-37, 1986.

[7] L. C. Hirst and N. J. Ekins-Daukes, "Fundamental losses in solar cells," *Progress in Photovoltaics,* vol. 19, pp. 286-293, 2011.

[8] T. Takagahara and K. Takeda, "Theory of the Quantum Confinement Effect on Excitons in Quantum Dots of Indirect-Gap Materials," *Physical Review B,* vol. 46, pp. 15578-15581, 1992.

[9] G. Conibeer, M. Green, E. C. Cho, D. Konig, Y. H. Cho, T. Fangsuwannarak, G. Scardera, E. Pink, Y. D. Huang, T. Puzzer, S. J. Huang, D. Y. Song, C. Flynn, S. Park, X. J. Hao, and D. Mansfield, "Silicon quantum dot nanostructures for tandem photovoltaic cells," *Thin Solid Films,* vol. 516, pp. 6748-6756, 2008.

[10] N. M. Park, T. S. Kim, and S. J. Park, "Band gap engineering of amorphous silicon quantum dots for light-emitting diodes," *Applied Physics Letters,* vol. 78, pp. 2575-2577, 2001.

[11] A. Kohno, H. Murakami, M. Ikeda, S. Miyazaki, and M. Hirose, "Memory operation of silicon quantum-dot floating-gate metal-oxide-

semiconductor field-effect transistors," *Japanese Journal of Applied Physics Part 2-Letters,* vol. 40, pp. L721-L723, 2001.
[12] G. Conibeer, M. Green, E.-C. Cho, D. König, Y.-H. Cho, T. Fangsuwannarak, G. Scardera, E. Pink, Y. Huang, T. Puzzer, S. Huang, D. Song, C. Flynn, S. Park, X. Hao, and D. Mansfield, "Silicon quantum dot nanostructures for tandem photovoltaic cells," *Thin Solid Films,* vol. 516, pp. 6748-6756, 2008.
[13] G. Conibeer, M. Green, R. Corkish, Y. Cho, E. C. Cho, C. W. Jiang, T. Fangsuwannarak, E. Pink, Y. D. Huang, T. Puzzer, T. Trupke, B. Richards, A. Shalav, and K. L. Lin, "Silicon nanostructures for third generation photovoltaic solar cells," *Thin Solid Films,* vol. 511, pp. 654-662, 2006.
[14] E. C. Cho, M. A. Green, G. Conibeer, D. Song, Y. H. Cho, G. Scardera, S. Huang, S. Park, X. J. Hao, Y. Huang, and L. V. Dao, "Silicon quantum dots in a dielectric matrix for all-silicon tandem solar cells," *Advances in OptoElectronics,* 2007.
[15] I. Perez-Wurfl, L. Ma, D. Lin, X. Hao, M. A. Green, and G. Conibeer, "Silicon nanocrystals in an oxide matrix for thin film solar cells with 492 mV open circuit voltage," *Solar Energy Materials and Solar Cells,* vol. 100, pp. 65-68, 2012.
[16] D. Y. Song, E. C. Cho, G. Conibeer, C. Flynn, Y. D. Huang, and M. A. Green, "Structural, electrical and photovoltaic characterization of Si nanocrystals embedded SiC matrix and Si nanocrystals/c-Si heterojunction devices," *Solar Energy Materials and Solar Cells,* vol. 92, pp. 474-481, 2008.
[17] Y. Cho and Y. H. E.-C. Cho, T. Trupke, G. Conibeer, and M. A. Green, "Silicon quantum dots in SiNx matrix for third generation photovoltaics," *Proceedings of the 20th European Photovoltaic Solar Energy Conference and Exhibition,* p. 47, 2005.
[18] M. Bouderbala, S. Hamzaoui, M. Adnane, T. Sahraoui, and M. Zerdali, "Annealing effect on properties of transparent and conducting ZnO thin films," *Thin Solid Films,* vol. 517, pp. 1572-1576, 2009.
[19] U. Ozgur, Y. I. Alivov, C. Liu, A. Teke, M. A. Reshchikov, S. Dogan, V. Avrutin, S. J. Cho, and H. Morkoc, "A comprehensive review of ZnO materials and devices," *Journal of Applied Physics,* vol. 98, 2005.
[20] T. R. Albrecht, S. Akamine, T. E. Carver, and C. F. Quate, "Microfabrication of Cantilever Styli for the Atomic Force Microscope," *Journal of Vacuum Science & Technology a-Vacuum Surfaces and Films,* vol. 8, pp. 3386-3396, 1990.
[21] Q. J. Cheng, S. Y. Xu, and K. Ostrikov, "Single-step, rapid

low-temperature synthesis of Si quantum dots embedded in an amorphous SiC matrix in high-density reactive plasmas," *Acta Materialia,* vol. 58, pp. 560-569, 2010.

[22] S. A. Studenikin, N. Golego, and M. Cocivera, "Optical and electrical properties of undoped ZnO films grown by spray pyrolysis of zinc nitrate solution," *Journal of Applied Physics,* vol. 83, pp. 2104-2111, 1998.

[23] Y. F. Chen, D. M. Bagnall, H. J. Koh, K. T. Park, K. Hiraga, Z. Q. Zhu, and T. Yao, "Plasma assisted molecular beam epitaxy of ZnO on c-plane sapphire: Growth and characterization," *Journal of Applied Physics,* vol. 84, pp. 3912-3918, 1998.

[24] Y. F. Li, B. Yao, Y. M. Lu, C. X. Cong, Z. Z. Zhang, Y. Q. Gai, C. J. Zheng, B. H. Li, Z. P. Wei, D. Z. Shen, X. W. Fan, L. Xiao, S. C. Xu, and Y. Liu, "Characterization of biaxial stress and its effect on optical properties of ZnO thin films," *Applied Physics Letters,* vol. 91, 2007.

[25] M. Oshikiri, Y. Imanaka, F. Aryasetiawan, and G. Kido, "Comparison of the electron effective mass of the n-type ZnO in the wurtzite structure measured by cyclotron resonance and calculated from first principle theory," *Physica B,* vol. 298, pp. 472-476, 2001.

[26] F. F. Wang, L. Cao, R. B. Liu, A. L. Pan, and B. S. Zou, "Photoluminescence and electroluminescence properties of ZnO films on p-type silicon wafers," *Chinese Physics,* vol. 16, pp. 1790-1795, 2007.

[27] X. J. Hao, E. C. Cho, C. Flynn, Y. S. Shen, S. C. Park, G. Conibeer, and M. A. Green, "Synthesis and characterization of boron-doped Si quantum dots for all-Si quantum dot tandem solar cells," *Solar Energy Materials and Solar Cells,* vol. 93, pp. 273-279, 2009.

[28] I. Perez-Wurfl, X. J. Hao, A. Gentle, D. H. Kim, G. Conibeer, and M. A. Green, "Si nanocrystal p-i-n diodes fabricated on quartz substrates for third generation solar cell applications," *Applied Physics Letters,* vol. 95, 2009.

[29] C. H. Cho, B. H. Kim, T. W. Kim, S. J. Park, N. M. Park, and G. Y. Sung, "Effect of hydrogen passivation on charge storage in silicon quantum dots embedded in silicon nitride film," *Applied Physics Letters,* vol. 86, 2005.

[30] C. G. Van de Walle, "Hydrogen as a cause of doping in zinc oxide," *Physical Review Letters,* vol. 85, pp. 1012-1015, 2000.

[31] Y. B. Zhang, G. K. L. Goh, K. F. Ooi, and S. Tripathy, "Hydrogen-related n-type conductivity in hydrothermally grown epitaxial ZnO films," *Journal of Applied Physics,* vol. 108, 2010.